On the resolution of shallow mantle viscosity structure using postearthquake relaxation data: Application to the 1999 Hector Mine, California, earthquake

Fred F. Pollitz[1] and Wayne Thatcher[1]

Received 27 January 2010; revised 1 June 2010; accepted 25 June 2010; published 15 October 2010.

[1] Most models of lower crust/mantle viscosity inferred from postearthquake relaxation assume one or two uniform-viscosity layers. A few existing models possess apparently significant radially variable viscosity structure in the shallow mantle (e.g., the upper 200 km), but the resolution of such variations is not clear. We use a geophysical inverse procedure to address the resolving power of inferred shallow mantle viscosity structure using postearthquake relaxation data. We apply this methodology to 9 years of GPS-constrained crustal motions after the 16 October 1999 M = 7.1 Hector Mine earthquake. After application of a differencing method to isolate the postearthquake signal from the "background" crustal velocity field, we find that surface velocities diminish from ~20 mm/yr in the first few months to $\lesssim$2 mm/yr after 2 years. Viscoelastic relaxation of the mantle, with a time-dependent effective viscosity prescribed by a Burgers body, provides a good explanation for the postseismic crustal deformation, capturing both the spatial and temporal pattern. In the context of the Burgers body model (which involves a transient viscosity and steady state viscosity), a resolution analysis based on the singular value decomposition reveals that at most, two constraints on depth-dependent steady state mantle viscosity are provided by the present data set. Uppermost mantle viscosity (depth $\lesssim$ 60 km) is moderately resolved, but deeper viscosity structure is poorly resolved. The simplest model that explains the data better than that of uniform steady state mantle viscosity involves a linear gradient in logarithmic viscosity with depth, with a small increase from the Moho to 220 km depth. However, the viscosity increase is not statistically significant. This suggests that the depth-dependent steady state viscosity is not resolvably different from uniformity in the uppermost mantle.

Citation: Pollitz, F. F., and W. Thatcher (2010), On the resolution of shallow mantle viscosity structure using postearthquake relaxation data: Application to the 1999 Hector Mine, California, earthquake, *J. Geophys. Res.*, *115*, B10412, doi:10.1029/2010JB007405.

1. Introduction

[2] The rheology of the crust and upper mantle controls the behavior of the lithosphere over the earthquake cycle of faulting at 10^2 to 10^3 years timescale and the transient response of the lithosphere to loading sources such as earthquakes and removal of lacustrine or ice loads. The relationship between time-dependent crustal deformation following such loading and the rheology has been used in numerous studies to infer the viscosity structure at depth below the brittle-ductile transition [e.g., *Hammond et al.*, 2008; *Bürgmann and Dresen*, 2008; *Thatcher and Pollitz*, 2008]. These models typically involve a strong (high-viscosity) lower crust underlain by a weak (low-viscosity) upper mantle, and this general pattern appears robust in actively deforming continental regions [e.g., *Thatcher and Pollitz*, 2008, Figure 3].

[3] Given the likely strong temperature dependence of viscosity, the question arises as to the finer-scale viscosity structure within the lower crust and shallow mantle. This is of particular concern in the uppermost mantle where laboratory-based models predict substantially higher viscosity than at greater depth. The models summarized in the above studies usually involve uniform viscosity in the lower crust and upper mantle, respectively, or models with very few distinct layers. In the context of postearthquake relaxation and relaxation following removal/filling of lacustrine loads, finer-scale viscosity structure has been addressed by forward modeling with allowance for several distinct layers or a continuum [e.g., *Bills et al.*, 1994a, 1994b; *Kaufmann and Amelung*, 2000; *Freed and Bürgmann*, 2004; *Freed et al.*, 2007; *Bills et al.*, 2007]. To our knowledge, apart from the sensitivity study of *Riva and Govers* [2009], the resolution of viscosity structure has not been addressed, and

[1]U.S. Geological Survey, Menlo Park, California, USA.

This paper is not subject to U.S. copyright.
Published in 2010 by the American Geophysical Union.

for the postearthquake relaxation problem it is not clear whether the available data adequately constrain vertical viscosity variations within the mantle.

[4] The formal resolution of mantle viscosity structure has been explored in the context of postglacial rebound by *Mitrovica and Peltier* [1991] and *Kendall and Mitrovica* [2007]. The investigation of *Kendall and Mitrovica* [2007] was motivated by the recognition [*Nakada and Lambeck*, 1989; *Lambeck and Nakada*, 1990] that available glacioisostatic adjustment data was sufficient to constrain more detail than either one or two-layer mantle models. Using a formal geophysical inverse approach, *Kendall and Mitrovica* [2007] showed that the data set considered by Nakada and Lambeck constrained essentially three independent mantle viscosity parameters.

[5] The purpose of this study is to address the resolution of shallow mantle viscosity structure using the detailed crustal motions measured by Global Positioning System (GPS) in the 9 years following the 16 October 1999 Hector Mine, California, earthquake. A wealth of regional GPS measurements are available, providing good spatial and temporal resolution of the postseismic crustal velocity field. We shall consider simple classes of viscoelastic stratification models that explain these data, including an evaluation of the resolution of mantle viscosity with depth.

2. Data Set

[6] We utilize time series of the Southern California Integrated GPS Network (SCIGN) made available by NASA through the REASoN Project (http://reason.scign.org/scignDataPortal/). We work with horizontal displacements of GPS data processed by the Scripps Orbit and Permanent Array Center (SOPAC). We use the "cleaned" time series without detrending resulting from the SOPAC processing. We consider postseismic crustal deformation in the 9 years following the 1999 Hector Mine earthquake at the same 88 GPS sites previously analyzed by *Freed et al.* [2007].

[7] We determine crustal velocity in distinct time intervals in two steps. In the first step, we estimate the seasonal terms of the time series and correct each time series for these terms. Specifically, for a postseismic time series $u(t)$ associated with a seismic event at time $t = 0$ (i.e., the origin time of the 1999 Hector Mine earthquake) we parameterize it as

$$u(t) = a_1 + a_2 * t + a_3 \log\left(1 + \frac{t}{\tau}\right) + a_4 \cos(2\pi t) + a_5 \sin(2\pi t) + a_6 \cos(4\pi t) + a_7 \sin(4\pi t). \quad (1)$$

The second term on the right-hand side of equation (1) represents the background velocity, and the third term represents the dominant component in the postseismic transient which typically has a logarithmic time dependence with a time constant $\tau \sim 0.1$ year [*Savage et al.*, 2005]. A value $\tau = 0.1$ year yields reasonable fits to all post-Hector Mine time series. The fourth through seventh terms on the right-hand side are seasonal terms with annual and semi-annual periods. Linear least squares inversion is used to determine the seven constants a_j from observations $u(t)$ at distinct times $t = t_i$; typically hundreds or thousands of time samples are used in such an inversion. The corrected time series is then

$$u_{\mathrm{obs}}(t) = u(t) - [a_4 \cos(2\pi t) + a_5 \sin(2\pi t) + a_6 \cos(4\pi t) + a_7 \sin(4\pi t)]. \quad (2)$$

[8] In the second step, we determine the average velocity within distinct time intervals. Observations $u_{\mathrm{obs}}(t_i)$ over a time interval (t_0, t_I) are fit with a model of quadratic time dependence

$$u_{\mathrm{mod}}(t) = b_0 + b_1(t - t_0) + b_2(t - t_0)^2. \quad (3)$$

Assuming white noise, for a given time series the constants b_0, b_1, and b_2 are found by minimizing the misfit function

$$\chi^2 = \sum_{i=0}^{I} \left(\frac{u_{\mathrm{obs}}(t_i) - u_{\mathrm{mod}}(t_i)}{\sigma_i} \right)^2, \quad (4)$$

where σ_i is the standard error in the observation. The average observed and model velocities over the time interval are

$$v_{\mathrm{obs}} = \frac{u_{\mathrm{obs}}(t_I) - u_{\mathrm{obs}}(t_0)}{t_I - t_0} \quad (5)$$

$$v_{\mathrm{mod}} = \frac{u_{\mathrm{mod}}(t_I) - u_{\mathrm{mod}}(t_0)}{t_I - t_0}. \quad (6)$$

It can be shown that if the true signal has a cubic dependence in time (i.e., constant third time derivative), then minimization of equation (4) provides an unbiased estimate of the average velocity. More precisely, if the observed signal were of the form $u_{\mathrm{obs}}(t) = c_0 + c_1(t - t_0) + c_2(t - t_0)^2 + c_3(t - t_0)^3$, then

$$E[v_{\mathrm{mod}}] = c_1 + c_2(t_I - t_0) + c_3(t_I - t_0)^2 = v_{\mathrm{obs}}, \quad (7)$$

where $E[]$ denotes expectation value.

[9] If a time series of length T is sampled at equally spaced intervals with independent, identically distributed errors (i.e., white noise), then for a given sample interval the theoretical error in estimated velocity scales as $T^{-3/2}$ [e.g., *Williams*, 2003]. However, a velocity estimation procedure that involves correlated noise (e.g., fractal random walk, flicker noise) yields standard deviations in interval velocities up to ~10 times larger than those resulting from the white noise model [*Langbein and Johnson*, 1997; *Zhang et al.*, 1997; *Mao et al.*, 1999]. In order to account for the presence of correlated noise, we scale up the formal velocity errors resulting from the white noise model by a factor of $(T/T_0)^{1/2}$, where T_0 is a reference timescale which we take equal to 1 year. The resulting velocity error scales as T^{-1} and is approximately that which would result from an interpretation of the time series error as flicker noise [*Mao et al.*, 1999; *Williams*, 2003]. For nonuniformly distributed time samples and variable sample errors, or for a noise model that includes other processes, both the estimated velocity and resulting velocity error would differ from our "scaled" white

noise estimates. A formal comparison between our procedure and a more rigorous one based on the complex statistics of geodetic time series [e.g., *Langbein*, 2004] could be illuminating but is beyond the scope of this paper. Meanwhile, our approximation provides a simple method of estimating the velocity errors in various time intervals and produces errors that we deem sufficient for our resolution analysis.

[10] Auxiliary Figures S1 and S2 show GPS time series at SCIGN sites AGMT and LDES, respectively, relative to reference model ITRF2005 [*Altamimi et al.*, 2007].[1] The seasonal terms are most pronounced in the vertical component, and most of the seasonal signal is removed by the procedure described above.

[11] Let $v^k_{\rm obs}$ and $v^k_{\rm mod}$ represent observed and modeled postseismic velocity in the kth time interval. The following time intervals (represented in terms of time following the Hector Mine earthquake) are deemed sufficient to capture the chief characteristics of the time-dependent postseismic velocity field: 2 weeks to 6 months (k = 1), 6 months to 1 year (k = 2), 1 year to 2 years (k = 3), 2 years to 5 years (k = 4), and 5 years to 9 years (k = 5). Figure S3 shows postseismic horizontal crustal velocity $v^k_{\rm obs}$ in these five time intervals.

[12] One complication in many previous studies [e.g., *Pollitz*, 2003; *Freed and Bürgmann*, 2004] is the need to independently specify the background tectonic velocity field, i.e., the motions that would occur in the absence of transient stressing from the Landers and Hector Mine events. *Pollitz* [2003] provided this by an estimate of the regional strain rates using pre-Landers data [*Savage and Svarc*, 1997]. Any such estimate is limited by the quality of pre-1992 data and the uncertain applicability beyond the area represented by that data. Here we avoid the need to deal explicitly with the background velocity field by working with differences in velocity between any two postseismic time intervals. This effectively removes the dependence of the tectonic background velocity on the postseismic velocity, facilitating an interpretation in terms of processes that are unique to the postseismic epoch. Toward this end, it is convenient to consider $v^k_{\rm obs}$ referred to the latest time interval being considered, i.e., 5 years to 9 years (k = 5).

[13] Figures 1 and S4 show the horizontal and vertical velocity components of the velocity fields defined by

$$\Delta v^k_{\rm obs} = v^k_{\rm obs} - v^5_{\rm obs}. \tag{8}$$

Figure 2a shows a spatially interpolated version of the vertical velocity field during the first 6 months. The horizontal velocity fields generally exhibit the spatial patterns expected for postseismic mantle relaxation following a crustal earthquake, e.g., a well-defined quadrant pattern [e.g., *Pollitz et al.*, 2001; *Pollitz*, 2003; *Freed and Bürgmann*, 2004]. Within ~100 km of the rupture, the vertical velocity field suggests a quadrant pattern in the vertical velocity field opposite to that produced by the coseismic deformation field (Figure 2a) but similar to that measured by InSAR [*Pollitz et al.*, 2001]. However, such signal is apparent only in the earliest considered time interval. For this early time period, a quadrant pattern is predicted for the vertical velocity field by a model of viscoelastic mantle relaxation (Figure 2b).

[14] A possible noise source in the data set is a baseline shift in velocity within a given time period, i.e., a constant velocity bias at all GPS stations. This could be related to a small time-dependent bias in the realization of ITRF2005 in the employed GPS time series (T. Herring, personal communication, 2009). The presence of such a signal in the horizontal velocity fields is suggested by the coherence patterns of observed time-dependent postseismic velocity. The coherence of the velocity fields in time intervals k_1 and k_2 is defined as

$$\text{coherence} = \frac{\left[\sum_n \sum_{l=1}^2 \Delta v^{k_1}_{\rm obs}(\hat{\mathbf{r}}_n, l)\Delta v^{k_2}_{\rm obs}(\hat{\mathbf{r}}_n, l)/(\sigma_{nl}(k_1)\sigma_{nl}(k_2))\right]^2}{\left(\sum_n \sum_{l=1}^2 \left[\Delta v^{k_1}_{\rm obs}(\hat{\mathbf{r}}_n, l)/\sigma_{nl}(k_1)\right]^2\right)\left(\sum_n \sum_{l=1}^2 \left[\Delta v^{k_2}_{\rm obs}(\hat{\mathbf{r}}_n, l)/\sigma_{nl}(k_2)\right]^2\right)}, \tag{9}$$

where $\sigma_{nl}(k)$ is the standard error in $\Delta v^k_{\rm obs}(\hat{\mathbf{r}}_n, l)$, the lth component of observed velocity at GPS site $\hat{\mathbf{r}}_n$ in the kth time interval. Figure 3 shows the coherence of velocity fields of the later three considered time periods with respect to the earliest time period (2 weeks to 6 months). This coherence is especially low for the 1 year to 2 years time interval, as may be verified visually by comparing the velocity fields in Figure 1. Correction of the velocity fields through application of a Helmert transformation with a magnitude of ~1 mm/yr acts to improve coherence substantially. The correction is justified on physical grounds, since candidate postseismic processes are expected to produce similar velocity patterns at different times, with primarily the amplitude, rather than the spatial pattern, varying with time. Small baseline shifts such as these are formally highly statistically significant, e.g., after subtracting a typical model velocity field, we find that residual variance for the 1 year to 2 year time interval is halved when the baseline shift in velocity is included. Since it is a constant velocity shift, it is independent of the background tectonic velocity field, which is spatially highly variable. We shall admit these baseline shifts in the postseismic deformation models, with the understanding that this is tantamount to modeling the strain rate field, rather than the velocity field.

[15] In subsequent modeling, we do not use the vertical velocity data. Although seasonal signals are to a large extent removed by the procedure described above, considerable errors remain in the differenced velocity fields, and these errors are long wavelength in nature (Figure S4). This may arise from nonseasonal errors specific to each time interval, such as those related to atmospheric or hydrologic signals. In any case, these nontectonic signals dominate over any tectonic signal that may be present. The analyses of succeeding sections have been carried out both with and without consideration of vertical velocity data, with almost

[1]Auxiliary materials are available in the HTML. doi:10.1029/2010JB007405.

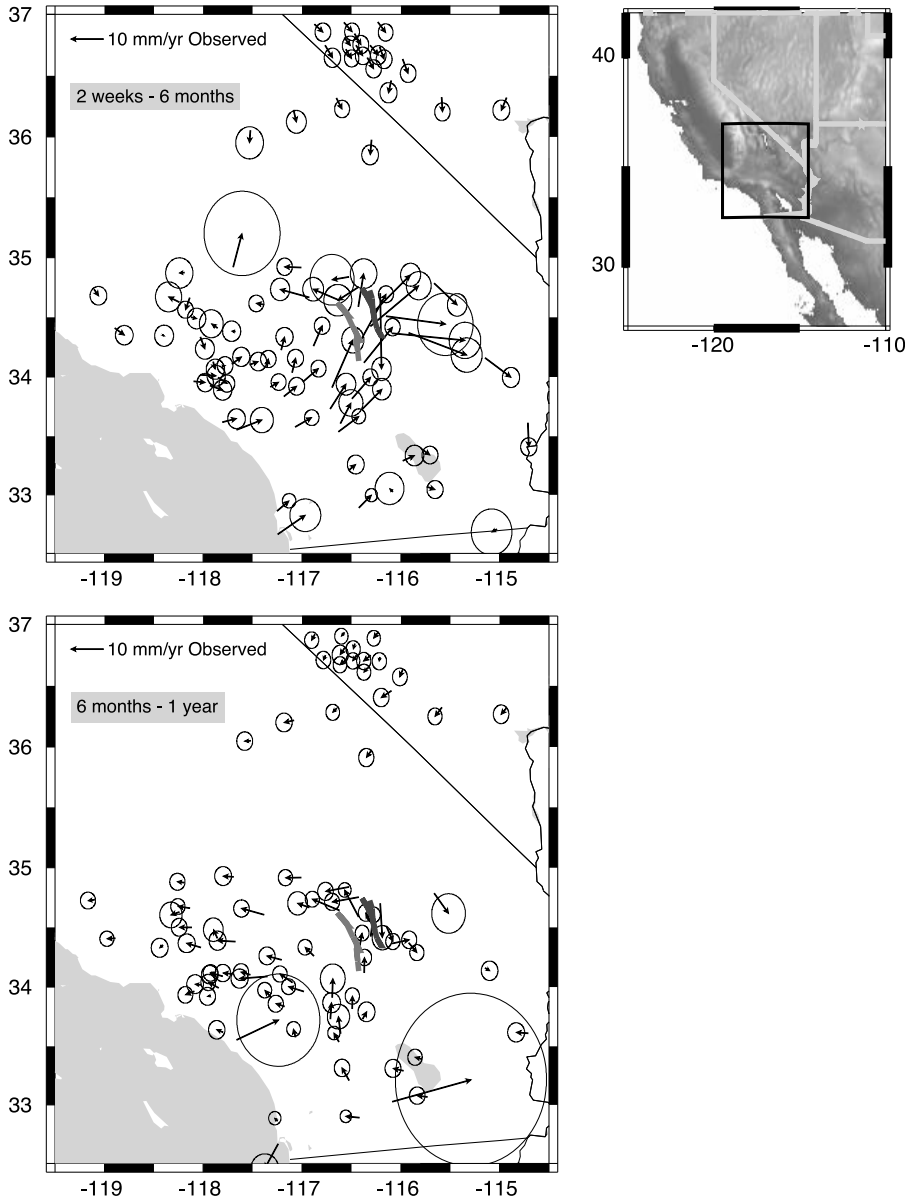

Figure 1. Observed differenced horizontal velocity fields $\Delta v^k_{\mathrm{obs}}$, defined as the difference between the observed velocity field in the indicated time interval minus that in the 5–9 years postseismic time interval. Error ellipses are 95% confidence regions. Thick light gray and dark gray lines are traces of the faults that ruptured in the 1992 Landers and 1999 Hector Mine earthquakes, respectively.

identical results, but for simplicity we present those derived without the vertical data.

3. Postseismic Deformation Model

[16] The postseismic velocity fields may be explained with a combination of postseismic processes, including poroelastic rebound [*Jónsson et al.*, 2003; *Fialko*, 2004], after slip [*Shen et al.*, 1996; *Savage and Svarc*, 1997; *Owen et al.*, 2002], and viscoelastic relaxation of the lower crust and upper mantle [*Pollitz et al.*, 2001; *Pollitz*, 2003; *Freed and Bürgmann*, 2004; *Freed et al.*, 2007]. As noted in previous work [*Pollitz et al.*, 2001; *Pollitz*, 2003], the pattern of observed vertical velocity rules out after slip as the dominant postseismic mechanism (its predicted vertical velocity field is anticorrelated with the observed vertical velocity field, see Figure 2), and the substantial horizontal velocity field (Figure 1) rules out poroelastic rebound as the dominant postseismic mechanism, as this mechanism alone produces relatively small horizontal motions. The combined poroelastic and after slip model proposed by *Fialko* [2004] for the 1992 Landers earthquake postseismic relaxation, however, is a strong candidate explanation for the joint observed horizontal and vertical velocity fields. One difficulty with the *Fialko* [2004] model is the need for high

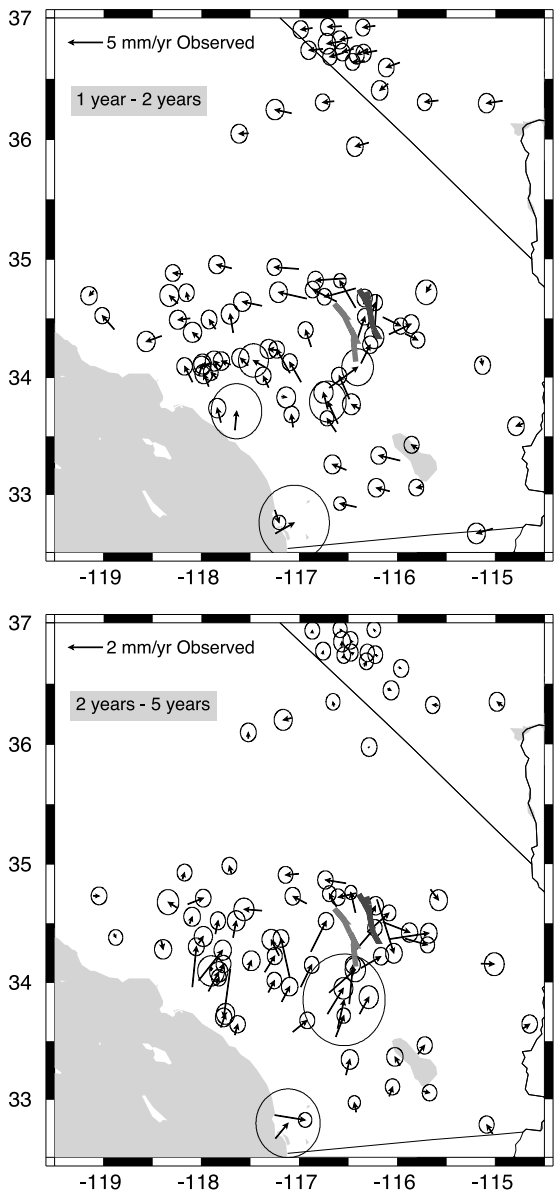

Figure 1. (continued)

permeability through the entire crust, a proposition that appears at odds with rapidly decreasing permeability in the upper 2–3 km based on laboratory studies and field data [*Ingebritsen and Manning*, 1999]. Another difficulty follows from the analysis of *Freed et al.* [2007], who showed that there is no viable alternative to viscoelastic relaxation of the mantle to explain the crustal motions of remote sites in the 7 years following the Hector Mine earthquake. A power law rheology with stress- and temperature-dependent viscosity suffices to explain these motions, and a substantial increase in effective mantle viscosity with time is necessary to capture the time dependence at remote sites.

[17] For a vertically stratified viscoelastic structure, postseismic crustal motions at Earth's surface are calculated using the methodology of *Pollitz* [1997]. The driving sources are the M7.3 1992 Landers and M7.1 1999 Hector Mine earthquakes. The fault models of *Wald and Heaton* [1994] and *Jónsson et al.* [2002] are adopted for the Landers and Hector Mine earthquakes, respectively. This yields average postseismic velocity v_{mod} (equation (6)) in selected time intervals as a function of the viscoelastic structure.

[18] In order to explain the data presented in Figure 1, we consider a sequence of models in order of increasing complexity. We adopt the viscoelastic stratification of Figure 4, which describes the lithosphere-asthenosphere system with a series of layers that permit a Burgers body rheology in the mantle [*Pollitz*, 2003]. The Maxwellian rheology depends on two parameters (in addition to the bulk modulus): the steady state shear modulus and viscosity. The Burgers body rheology depends on four parameters: the steady state shear modulus and viscosity (μ_1 and η_1, respectively) and the transient shear modulus and viscosity (μ_2 and η_2, respectively). The analog of the rheology is a Maxwell element in series with a Kelvin element. The Burgers body thus exhibits two relaxation times, $\tau_1 = \eta_1/\mu_1$ and $\tau_2 = \eta_2/\mu_2$. Assuming $\eta_2 \ll \eta_1$, the effective shear modulus μ' after relaxation of the Kelvin element is $\mu' = \mu_1\mu_2/(\mu_1 + \mu_2)$. This model is motivated by laboratory observations of two phases of relaxation, consisting of transient creep followed by primary (or steady state) creep [e.g., *Carter and Kirby*, 1978; *Ranalli*, 1987], characterized by a gradual increase in effective viscosity with time [e.g., *Post*, 1977].

[19] All models to be considered possess either an elastic lower crust or a lower crust of much higher viscosity than the average mantle viscosity. This starting point is justified based on results obtained from postseismic relaxation studies conducted in many continental regions [*Hammond et al.*, 2008; *Bürgmann and Dresen*, 2008; *Thatcher and Pollitz*, 2008], including the Mojave Desert. We explore the following classes of models: class I, purely elastic lower crust ($\eta_c = \infty$) and Maxwellian mantle (realized with $\mu_2 = \infty$); class II, purely elastic lower crust ($\eta_c = \infty$) and Burgers body mantle; and class III, Maxwell viscoelastic lower crust and Burgers body mantle.

[20] In section 4, misfit functions are defined in order to facilitate comparison of observations with models. In section 5 we consider the optimal models with uniform viscosity in the lower crust and mantle. In section 6, using the best class III uniform-viscosity model as a reference model, we compute numerical Fréchet derivatives with respect to perturbations in viscosity, then evaluate the resolution of depth-dependent mantle viscosity with a geophysical inverse procedure. In section 7, using the same inverse approach, we infer depth-dependent mantle viscosity of all three model classes and compare their performance among one another and with the corresponding uniform viscosity models.

4. Misfit Functions

[21] As with the observed velocity fields defined with equation (8), we define a similar quantity for the modeled velocities:

$$\Delta v^k_{\mathrm{mod}} = v^k_{\mathrm{mod}} - v^5_{\mathrm{mod}}. \tag{10}$$

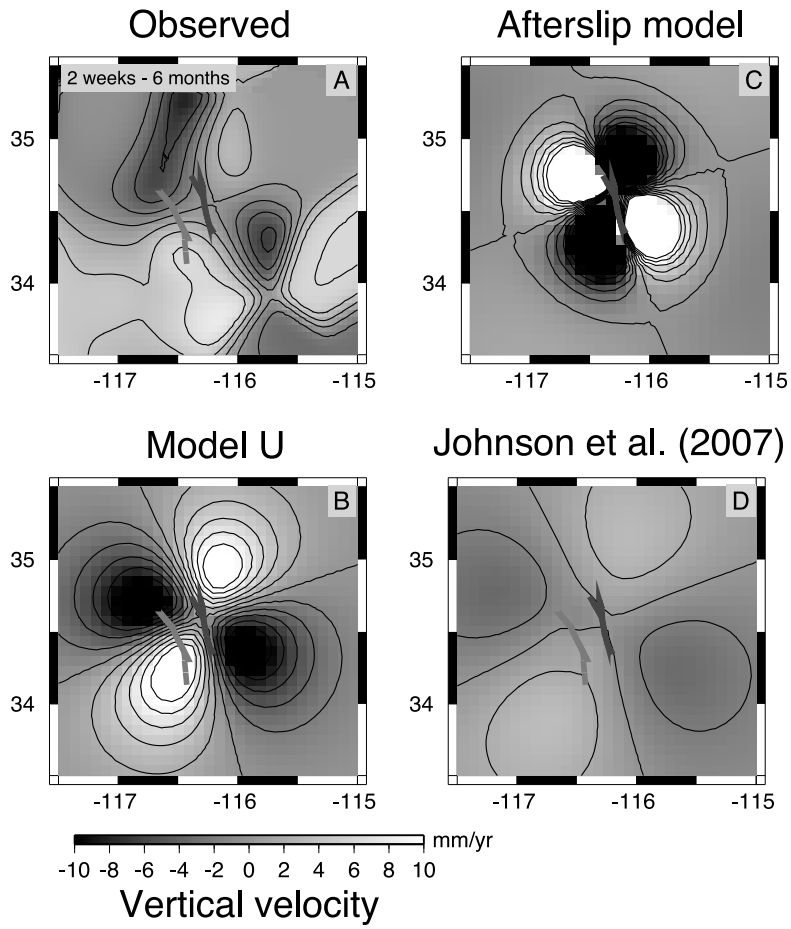

Figure 2. (a) Differenced vertical velocity field in the time interval 2 weeks to 6 months after the Hector Mine earthquake, derived by isotropic interpolation from Figure S4. (b) Corresponding prediction of model U (section 5.2). (c) Corresponding prediction of after slip model (section 8.5) (d) Corresponding prediction of the *Johnson et al.* [2007] model (section 8.5).

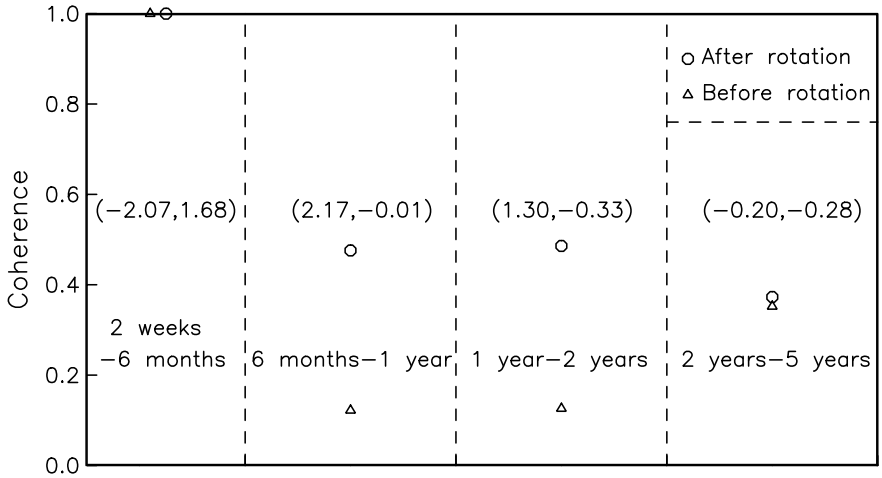

Figure 3. Coherence of observed velocity fields in the indicated time intervals with the observed velocity field in the earliest considered time period (2 weeks to 6 months). Values are given both before and after application of a Helmert transformation, which is to a high degree of approximation a constant velocity shift with the indicated values (east velocity shift followed by north velocity shift in mm/yr) in each respective time period. The Helmert transformation used in this example was derived by fitting a time-dependent uniform mantle viscosity model jointly with Helmert transformation parameters to the observed velocity fields (see section 5.2).

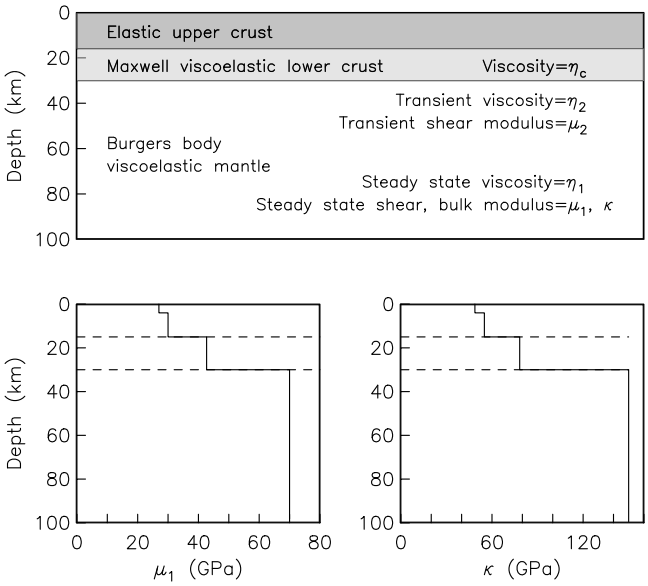

Figure 4. Viscoelastic stratification assumed for the Mojave Desert (model used here following *Pollitz* [2003, Figures 5a and 5c]). Elastic parameters μ_1 and κ are the steady state shear modulus and bulk modulus, respectively. Elastic and viscoelastic parameters are constant in the mantle (depth >30 km). This structure represents the class III model introduced in section 3.

We define the misfit function at GPS site $\hat{\mathbf{r}}_n$ for the lth velocity component (where l = 1 and 2 denote the local east and north directions) and kth time interval as

$$\chi_l^2(k) = \sum_n \frac{\left[\Delta v_{\mathrm{mod}}^k(\hat{\mathbf{r}}_n, l; \mathbf{v}) - v_l^{(k)}(\hat{\mathbf{r}}_n) - \Delta v_{\mathrm{obs}}^k(\hat{\mathbf{r}}_n, l)\right]^2}{[\sigma_{nl}(k)]^2}, \quad (11)$$

where $\mathbf{v}$ represents viscoelastic model parameters and $v_l^{(k)}(\hat{\mathbf{r}}_n)$ is the baseline shift in velocity represented by Helmert transformation parameters. All inversions in the following sections shall involve solving for one or more unknown viscoelastic parameters as well as a set of Helmert transformation parameters (three parameters per time period) for the horizontal components (l = 1, 2). Each Helmert transformation typically involves a remote rotation pole, so that the baseline shifts $v_1^{(k)}(\hat{\mathbf{r}}_n)$ and $v_2^{(k)}(\hat{\mathbf{r}}_n)$ are practically independent of station position $\hat{\mathbf{r}}_n$.

[22] We define the normalized root-mean-square misfit in time interval k as

$$\mathrm{NRMS}(k) = \sqrt{\left(\chi_1^2(k) + \chi_2^2(k)\right)^2 / 2N_h(k)}, \quad (12)$$

where $N_h(k)$ is the number of GPS sites contributing data in the considered time interval. Related misfit functions are those summed over all time intervals:

$$\chi_{\mathrm{total}}^2 = \sum_k \left[\chi_1^2(k) + \chi_2^2(k)\right] \quad (13)$$

$$\mathrm{NRMS(total)} = \sqrt{\chi_{\mathrm{total}}^2 / 2N_h}, \quad (14)$$

where $N_h = \Sigma_k N_h(k)$. (We do not use these NRMS for statistical tests; the appropriate quantity for that would be NRMS (total) = $\sqrt{\chi_{\mathrm{total}}^2/(2N_h - M)}$, where M is the number of model parameters.)

5. Uniform Viscosity Models

5.1. Maxwell Model

[23] We consider the performance of class I models in which the predicted velocity field depends only on steady state mantle viscosity η_1. Figure 5 shows the resulting misfit as a function of η_1. The predicted horizontal velocity field at the optimal value $\eta_1 = 4.6 \times 10^{18}$ Pa s (Figure S5) illustrates a fundamental limitation of the Maxwell model: because of the single time constant τ_1 = 4.8 years, observed horizontal velocity is underpredicted at early times and overpredicted at later times. This limitation has been noted in several previous studies [*Pollitz et al.*, 2001; *Pollitz*, 2003; *Freed and Bürgmann*, 2004; *Freed et al.*, 2007]. The misfit at the optimal viscosity (Figure 6 and Table 1) is systematically larger than that of other models that we shall consider. The misfit may be improved substantially by allowing for time-dependent viscosity in the mantle, as is prescribed by either a nonlinear (stress and temperature-dependent rheology) or a higher-order linear rheology.

5.2. Burgers Body Model

[24] The Jeffreys fluid [*Ivins*, 1996] is the simplest linear rheology that accommodates two material relaxation times. It is a special case of a Burgers body in which $\mu_1 = \mu_2$. This is represented here by model classes II and III introduced in section 3. *Pollitz* [2003] obtained optimal model parameters of class III (with uniform viscosities in the respective lower crust and mantle domains) by performing a grid search and evaluating misfit of horizontal and vertical postseismic velocity in selected time intervals up to 2.5 years after the Hector Mine earthquake.

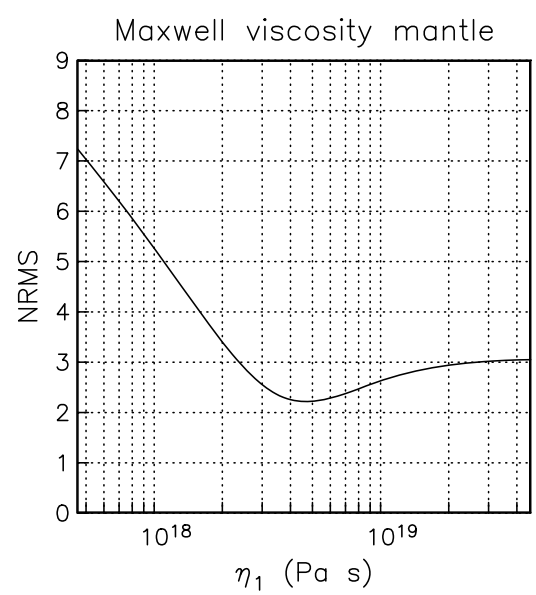

Figure 5. NRMS (total) (equation (14)) with respect to Maxwell viscosity models as a function of mantle viscosity.

Table 1. NRMS of Selected Models to Postseismic Velocity Data

Time Period	Null Model	Uniform Viscosity Mantle[a]	Constant Viscosity Gradient[b]	Layered Mantle[c]	Mantle Lid[d]	Maxwell Viscosity Mantle[e]	*Johnson et al.* [2007][f]
2 weeks to 6 months	3.79	1.70	1.69	1.68	1.84	2.31	3.19
6 months to 1 year	2.37	1.65	1.62	1.62	1.71	1.49	1.99
1 year to 2 years	2.82	1.77	1.74	1.72	1.82	2.05	2.24
2 years to 5 years	3.42	2.45	2.46	2.45	2.49	3.16	2.78
2 weeks to 5 years	6.06	3.25	-	-	3.32	4.49	4.34

[a]Model U, described in section 5.2 (plotted in Figure 8a).
[b]Class III model described in section 7.1 (plotted in Figure 8b).
[c]Class III model described in section 7.2 (plotted in Figure 8c).
[d]Mantle lid model described in section 8.5 (plotted in Figure 8d).
[e]Class I model described in section 5.1.
[f]Southern San Andreas fault model described in section 8.5.

[25] We repeat this grid search using the data and four time intervals represented in Figure 1 using the misfit measure $\chi_l^2(k)$, evaluated for horizontal components. Figure 7 shows the resulting misfit patterns for the horizontal components. We choose a best fitting model, henceforth model U, with parameters $\eta_1 = 3.7 \times 10^{18}$ Pa s, $\eta_2 = 1.0 \times 10^{17}$ Pa s, $\mu' = 0.5 \times \mu_1$ and $\eta_c = 2.6 \times 10^{19}$ Pa s $= 7 \times \eta_1$.This model, which is close to the best fitting model determined by *Pollitz* [2003], provides a good fit to the velocity data through a postseismic time period twice as long as that considered by *Pollitz* [2003] (5 years versus 2.5 years) and with no arbitrary explicit or implicit assumptions about the unknown steady state velocity field. This model is shown in Figure 8a, and the corresponding fits to the data are shown in Figure 9; NRMS of horizontal velocity data within specific time periods are listed in Table 1.

[26] In separate inversions (not shown), there is little sensitivity of the vertical velocity data to the viscosity structure at times beyond 6 months and marginal sensitivity to viscosity structure during the first 6 months. This reflects a generally poor signal-to-noise ratio for the vertical data, which diminishes with time in step with the magnitude of postseismic relaxation. Comparison of the observed and model U vertical velocity field during the first 6 months (Figure 2b) indicates a modest correlation (correlation coefficient = 0.25), with both exhibiting a quadrant pattern characteristic of mantle stress relaxation [e.g., *Pollitz et al.*, 2001].

[27] Another model worthy of consideration is shown by square symbols in Figure 7 and has parameters $\eta_1 = 6.0 \times 10^{19}$ Pa s, $\eta_2 = 4.6 \times 10^{18}$ Pa s, $\mu' = 0.5 \times \mu_1$ and $\eta_c = 4.2 \times 10^{20}$ Pa s $= 7 \times \eta_1$. This rheological model is one of several relatively low-misfit models that lie along a line of approximately constant η_2 near the above value. It involves steady state and transient viscosity values more than 10 times greater than those of model U. Compared with model U it is associated with similar NRMS in the later three time periods but somewhat larger NRMS in the 2 weeks to 6 months period (NRMS = 2.62 versus NRMS = 1.70 in model U). The predictions of model U and this alternative model and comparison with observed time series are shown in Figure 10. In Figure 10, both observed and theoretical time series are referenced to their respective average velocities in the 5–9 years time interval; a baseline velocity shift has been further added to the observed time series. The alternative model yields roughly the same interval velocities as model U beyond the first half year but generally cannot match the

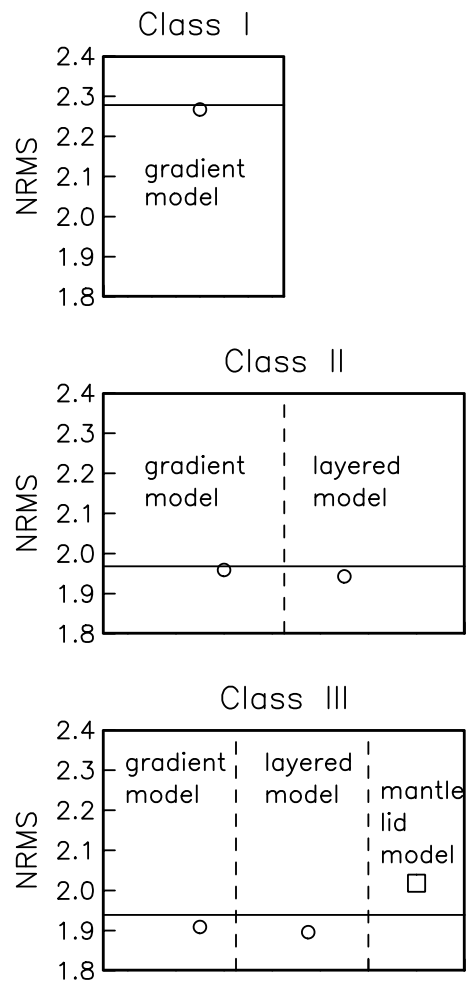

Figure 6. NRMS (total) (equation (14)) of viscoelastic relaxation models. The gradient and layered models are those presented in sections 7.1 and 7.2, respectively. Horizontal lines indicate the misfit associated with the given model class assuming uniform viscosities in the respective lower crust and upper mantle domains. Circles represent the viscosity structure from inversions for depth-dependent η_1 with other parameters fixed. Squares represent the viscosity structure (on model class III only) resulting from a grid search for optimal mantle viscosity parameters including a high-viscosity mantle lid (see section 8.5).

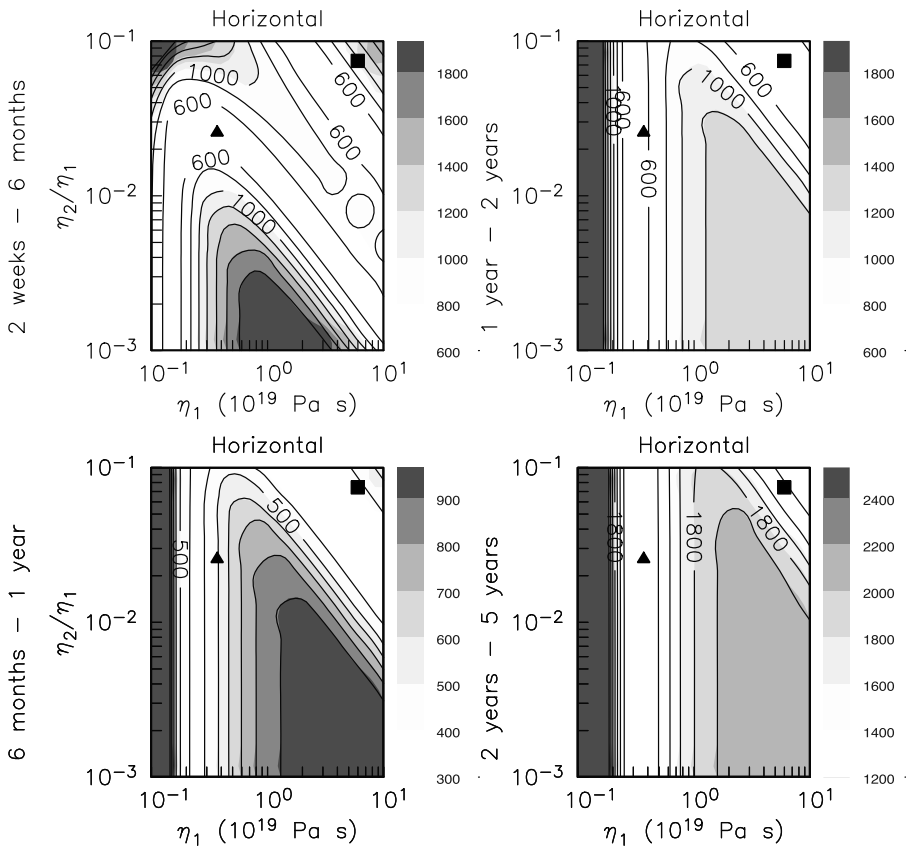

Figure 7. The χ^2_{total} misfit of horizontal velocity data with respect to class III Burgers body models with various combinations of η_1 and η_2/η_1. Results are shown for four different time intervals. Relaxed shear modulus $\mu' = 0.5 \times \mu_1$ and ratio $\eta_c/\eta_1 = 7$ are fixed in all models. Black triangle indicates the best fitting model over all time intervals, with parameters $\eta_1 = 3.7 \times 10^{18}$ Pa s, $\eta_2 = 1.0 \times 10^{17}$ Pa s, $\mu' = 0.5 \times \mu_1$ and $\eta_c = 2.6 \times 10^{19}$ Pa s $= 7 \times \eta_1$. Black square indicates alternative model with parameters $\eta_1 = 6.0 \times 10^{19}$ Pa s, $\eta_2 = 4.6 \times 10^{18}$ Pa s, $\mu' = 0.5 \times \mu_1$ and $\eta_c = 4.2 \times 10^{20}$ Pa s $= 7 \times \eta_1$.

curvature of postseismic time series during the first half year. If part of the motion in the earliest time period could be ascribed to after slip, then this relatively high-viscosity model would be a plausible alternative to the chosen uniform-viscosity model.

[28] Additional searches with other trial values of μ' and η_c/η_1 generally yield poorer fits to the data. For example, we repeated the grid search with $\eta_c = \infty$, i.e., the class II model, and obtain the identical values for optimal η_1 and η_2 but with slightly larger misfits of the horizontal data subsets relative to class III (Figure 6). An F test using the class II and III uniform-viscosity models suggests that the addition of a finite lower crust viscosity in the class III model is statistically significant at 74% confidence. This is a marginal improvement and reflects the fact that the data set is likely too short to detect much lower crust relaxation. Choosing class III, the viscosity structure prescribed by model U serves as a useful "uniform" reference model for the velocity data considered in the present study.

6. Resolving Power of Postearthquake Data

[29] The interpretation of inferred viscosity structures from inversions of postearthquake data should be based on the formal resolving power of the data set. For this purpose, using the data set of postearthquake deformation after the 1999 Hector Mine earthquake (section 2), we set up a regularized inversion problem for depth-dependent perturbations in logarithmic steady state viscosity about a reference structure, employing a number of layers of uniform thickness. Radially variable mantle viscosity is implemented through perturbation theory in a series of definite depth intervals. The layering is represented with radius intervals $\{(r_1^{(j)}, r_2^{(j)}), j = 1, 19\}$, each of thickness 10 km spanning the range 30–220 km depth. We define $\mathbf{p}_0$ as the uniform viscosity structure given by model U (section 5.2) and $\mathbf{p}_j$ as $\mathbf{p}_0$ modified for the perturbed viscosity profile given by

$$\eta_1^{(j)}(r) = \begin{cases} \eta_1^{\text{uniform}} & r > r_2^{(j)}, \\ 1.1 \times \eta_1^{\text{uniform}} & r_2^{(j)} \geq r > r_1^{(j)}, \\ \eta_1^{\text{uniform}} & r \leq r_1^{(j)}, \end{cases} \tag{15}$$

where η_1^{uniform} is the mantle viscosity in model U.

[30] For a viscoelastic model $\mathbf{v}$, recall that $\Delta v^k_{\text{mod}}(\hat{\mathbf{r}}_n, l; \mathbf{v})$ is the differenced model velocity field on $\mathbf{v}$. Let $\mathbf{p}$ be the profile of perturbed steady state viscosity parameterized as

$$\ln \eta_1(r) = \ln \eta_1^{\text{uniform}} + \sum_j m_j \left[\ln \eta_1^{(j)}(r) - \ln \eta_1^{\text{uniform}} \right], \tag{16}$$

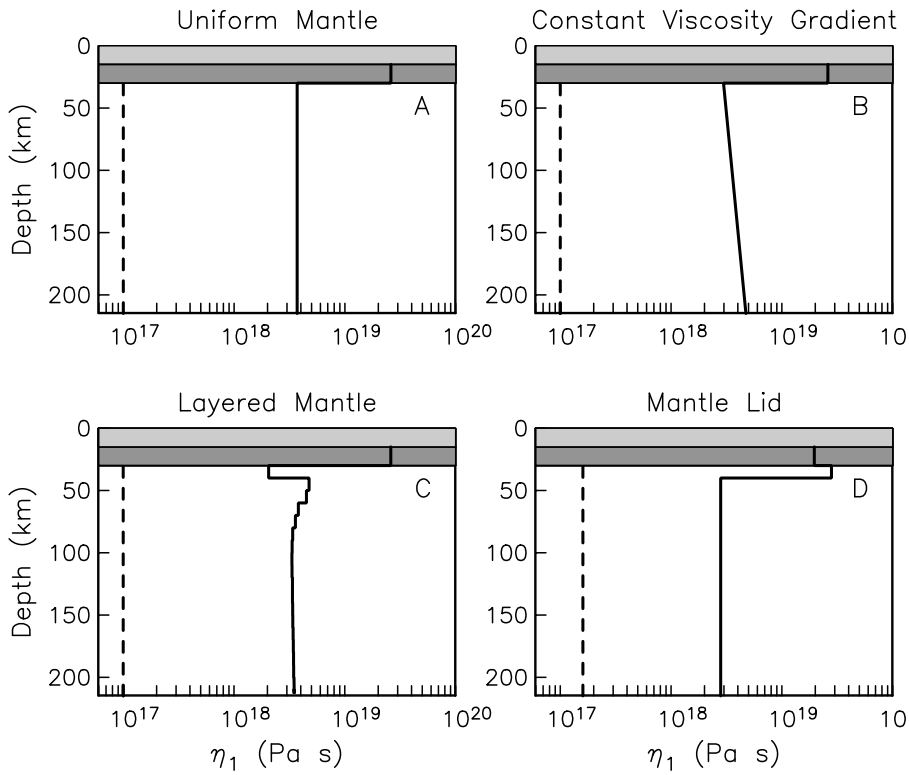

Figure 8. Viscoelastic structure of selected models. (a) The uniform-viscosity Burgers body model derived in section 5.2 (model U, based on grid search presented in Figure 7). (b) The constant-gradient model derived in section 7.1 (class III model shown in Figure 13). (c) The layered model derived in section 7.2 (class III model shown in Figure 14). (d) The mantle lid model derived in section 8.5 (based on grid search presented in Figure S6). In all cases, the dashed line indicates the transient mantle viscosity η_2.

where the $\{m_j\}$ are unknown parameters. The differenced model velocity on $\mathbf{p}$ is then

$$\Delta v^k_{\mathrm{mod}}(\hat{\mathbf{r}}_n, l; \mathbf{p}) = \Delta v^k_{\mathrm{mod}}(\hat{\mathbf{r}}_n, l; \mathbf{p}_0) + \sum_j m_j \times \partial_{\epsilon_j} \Delta v^k_{\mathrm{mod}}(\hat{\mathbf{r}}_n, l; \mathbf{v})|_{\mathbf{v}=\mathbf{p}}, \tag{17}$$

where ϵ_j refers to logarithmic viscosity in the jth layer and the Fréchet derivative is evaluated numerically, e.g., at $\mathbf{v} = \mathbf{p}_0$ it is

$$\partial_{\epsilon_j} \Delta v^k_{\mathrm{mod}}(\hat{\mathbf{r}}_n, l; \mathbf{v})|_{\mathbf{v}=\mathbf{p}_0} = \frac{\left[\Delta v^k_{\mathrm{mod}}(\hat{\mathbf{r}}_n, l; \mathbf{p}_j) - \Delta v^k_{\mathrm{mod}}(\hat{\mathbf{r}}_n, l; \mathbf{p}_0)\right]}{\ln(1.1)}. \tag{18}$$

[31] As the results shall bear out, the number of independent constraints on the steady state viscosity in the mantle is between 1 and 2. Since the model space has 19 degrees of freedom, it is necessary to regularize the inversion. We choose to do this by damping the mean squared amplitude of vertical viscosity variations with a damping weight β^2, i.e.,

$$\beta^2 \sum_j m_j^2. \tag{19}$$

This quantity is added to the misfit function χ^2_{total} given in equation (13).

[32] With the misfit function defined by equations (13) and (19), the least squares solution of the inverse problem for the model vector of viscosity perturbations $\mathbf{m}$ has the form [*Menke*, 1989]

$$\mathbf{m} = \left(\mathbf{G}^T\mathbf{C}^{-1}\mathbf{G} + \beta^2\mathbf{I}\right)^{-1}\mathbf{G}^T\mathbf{C}^{-1}\mathbf{d}, \tag{20}$$

where $\mathbf{G}$ is the matrix of Fréchet derivatives and $\mathbf{C}$ is the data covariance matrix. Since the Fréchet derivatives depend on the model itself, the inverse problem solved by equation (20) is nonlinear. Although an iterative approach is warranted for nonlinear problems [e.g., *Kaufmann and Lambeck*, 2000; *Kendall and Mitrovica*, 2007], we assume that the reference structure (i.e., model U) is sufficiently close to the optimal Burgers body model that linearity with respect to perturbations in logarithmic viscosity is satisfied. That is,

$$\partial_{\epsilon_j} \Delta v^k_{\mathrm{mod}}(\hat{\mathbf{r}}_n, l; \mathbf{v})|_{\mathbf{v}=\mathbf{p}} \approx \partial_{\epsilon_j} \Delta v^k_{\mathrm{mod}}(\hat{\mathbf{r}}_n, l; \mathbf{v})|_{\mathbf{v}=\mathbf{p}_0}. \tag{21}$$

This approach is consistent with the small perturbations in the derived models, and it is sufficient to demonstrate the resolving power of the postearthquake data set. A case involving a large viscosity perturbation (a strong mantle lid) will be considered separately in section 8.5.

[33] We choose the damping constant given by $1/\beta = 0.2$, corresponding to an a priori standard error in logarithmic viscosity of 0.2 in every layer. We find by trial and error that this choice of $1/\beta$ is the smallest that can be made that keeps

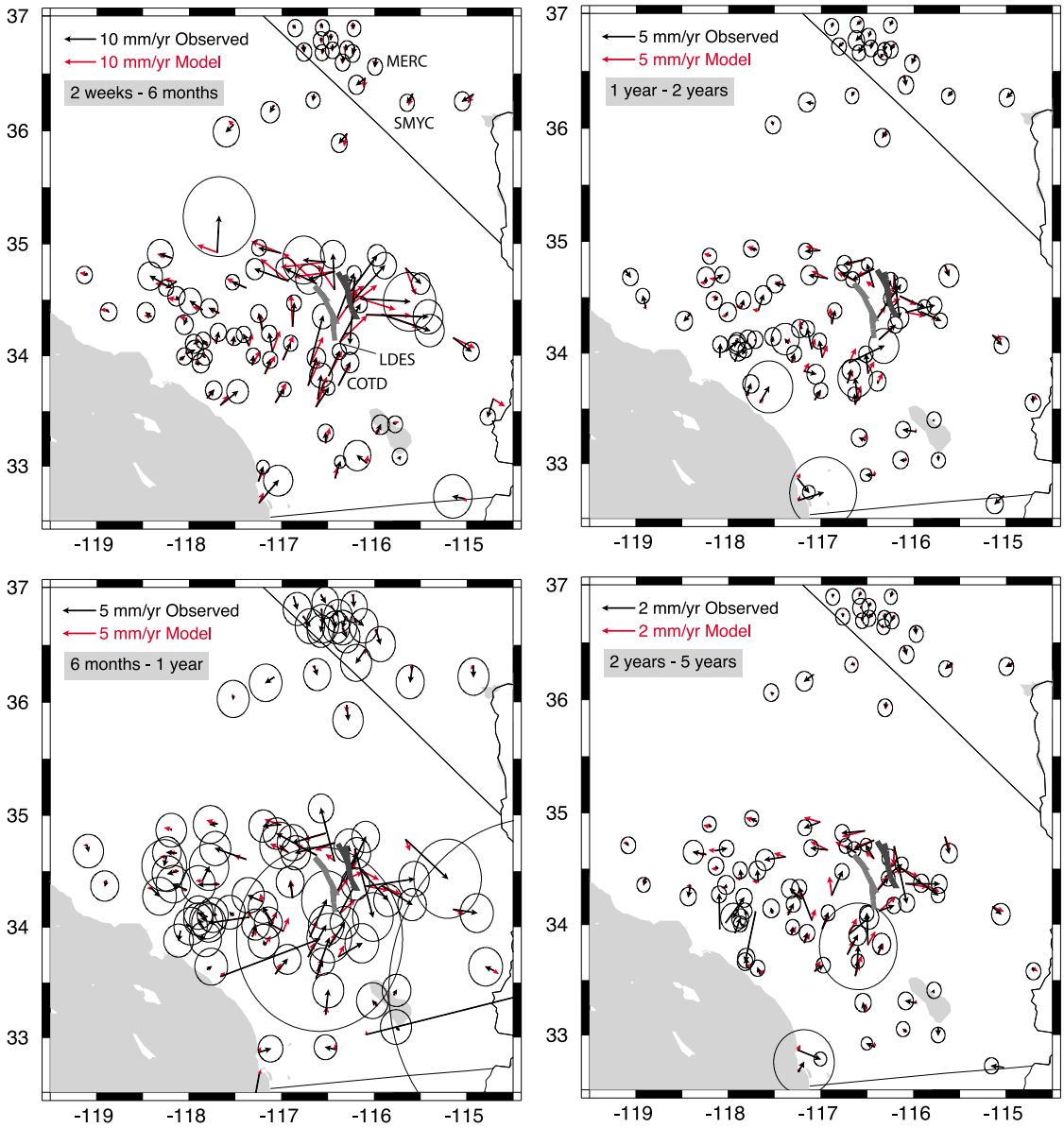

Figure 9. Observed differenced horizontal velocity fields $\Delta v^k_{\rm obs}$, given by equation (8) and corrected for a baseline shift of amount $-v_l^{(k)}(\hat{\mathbf{r}}_n)$ (equation (11)). Error ellipses are 95% confidence regions. Red vectors are the corresponding predictions $\Delta v^k_{\rm mod}$ of model U (section 5.2).

resulting viscosity perturbations bounded below a factor of two, i.e., $|\ln(\eta_1) - \ln \eta_1^{\rm uniform}| \lessapprox 0.7$. Smaller choices of $1/\beta$ yield only slightly smaller residual variance at the expense of large viscosity fluctuations with depth, which we deem unrealistic.

[34] Evaluation of equation (20) using the approach of singular value decomposition (SVD) [*Menke*, 1989] yields the $\{m_j\}$ and hence the depth distribution of η_1, the eigenvalues and eigenvectors of the SVD, and the model resolution matrix. The latter is given by

$$\mathbf{R} = \left(\mathbf{G}^T\mathbf{C}^{-1}\mathbf{G} + \beta^2\mathbf{I}\right)^{-1}\mathbf{G}^T\mathbf{C}^{-1}\mathbf{G}. \tag{22}$$

To evaluate the resolution, we restrict attention to the class III model (i.e., Burgers body mantle rheology with a relaxing lower crust) and consider viscosity structures in which the steady state mantle viscosity η_1 is permitted to vary with depth, while all other viscoelastic parameters, η_2, μ_2, μ', η_c (Figure 4), are fixed at the optimal values given in 5.2.

[35] The trace of the resolution matrix provides a measure of the number of independent parameters resolved by the data [*Wiggins*, 1972]. We find tr(**R**) = 1.6, so that the postearthquake data set constrains at most two independent constructs of mantle viscosity. Figure 11 shows the eigenvalue spectrum and eigenvectors of the SVD associated with the two largest eigenvalues resulting from application to the class III viscosity structure, and Figure 12 shows the model resolution for input mantle viscosity variations in successive 10 km thick sections between 30 and 120 km depth. (In these examples, we employ inversions that exclude the

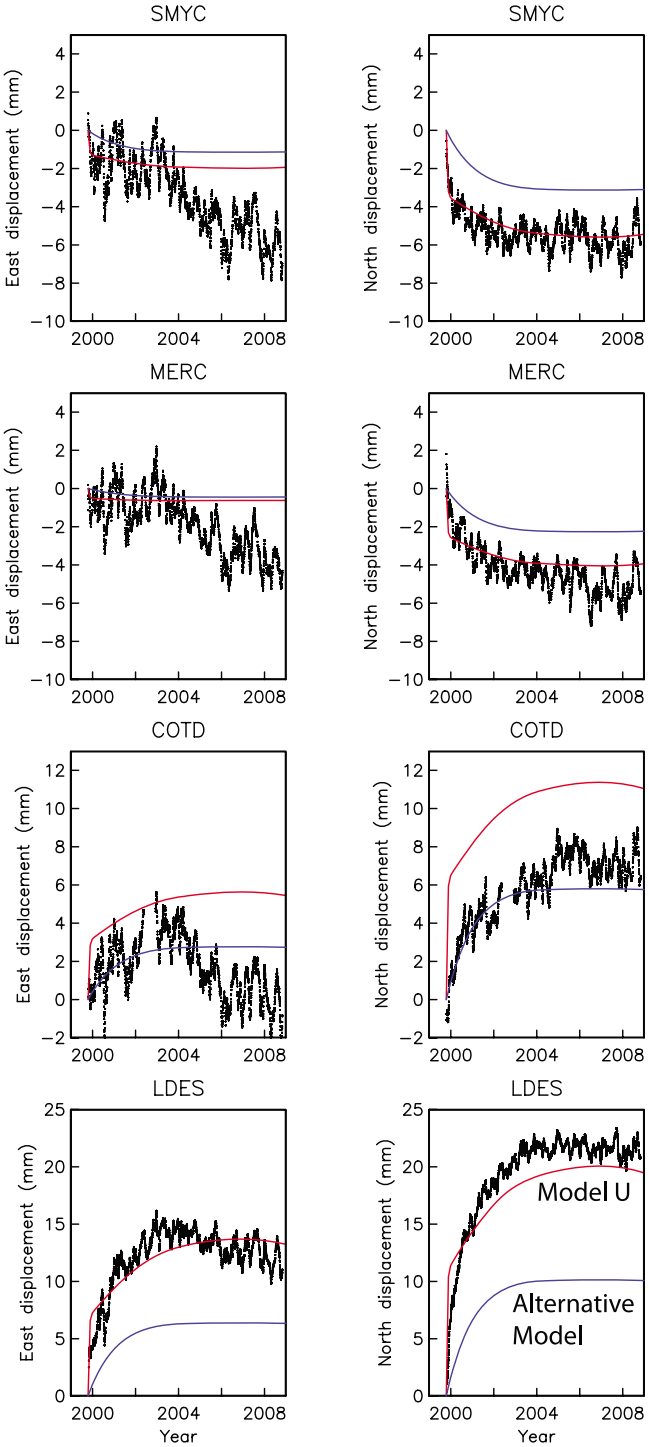

Figure 10. Time series of four sites (locations indicated in Figure 9 and 18) plotted with 19 day moving averages of observed time series. The observed time series have been corrected for the baseline velocity shift in the 2 weeks to 5 years time interval (section 8.1). Red curves are the prediction of model U (triangles in Figure 7), and blue curves are the prediction of an alternative model (squares in Figure 7).

Helmert transformation parameters (section 4) in order to isolate the sensitivity to mantle layer parameters.) Only the first two eigenvalues contribute substantially to the overall solution, indicating that the best sensitivity is in the upper ~20–30 km of the mantle (50–60 km depth). This is confirmed by the model resolution, which suggests that actual vertical viscosity variations may be marginally resolved down to ~60 km depth. Results are not sensitive to the details of the assumed rheological model. For example, qualitatively similar results are obtained from the corresponding inversion for class II mantle viscosity structure.

7. Depth-Dependent Mantle Viscosity Structure

[36] The preceding methods are applied to infer the depth-dependent viscosity structure beneath the source region of the 1999 Hector Mine earthquake using the postearthquake data set described in section 2. We consider viscosity structures in which the steady state mantle viscosity η_1 is permitted to vary with depth, while all other viscoelastic parameters, η_2, μ_2, μ', η_c (Figure 4), are fixed at the optimal values given in section 5.1 or 5.2, according to whether the mantle rheology is Maxwell viscoelastic or a Burgers body.

7.1. Viscosity Gradient in the Mantle

[37] For all three model classes, we consider the case where mantle viscosity is not uniform but rather has a constant gradient with depth. To this end, let γ be a vertical

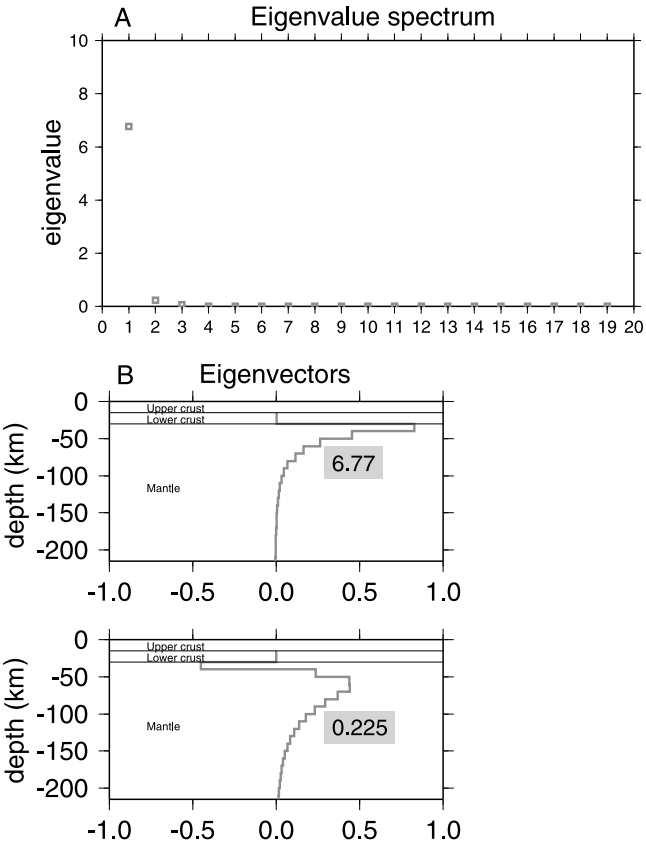

Figure 11. (a) Eigenvalue spectrum of the singular value decomposition for layered steady state mantle viscosity, using the class III model. (b) Eigenvectors associated with the two highest eigenvalues.

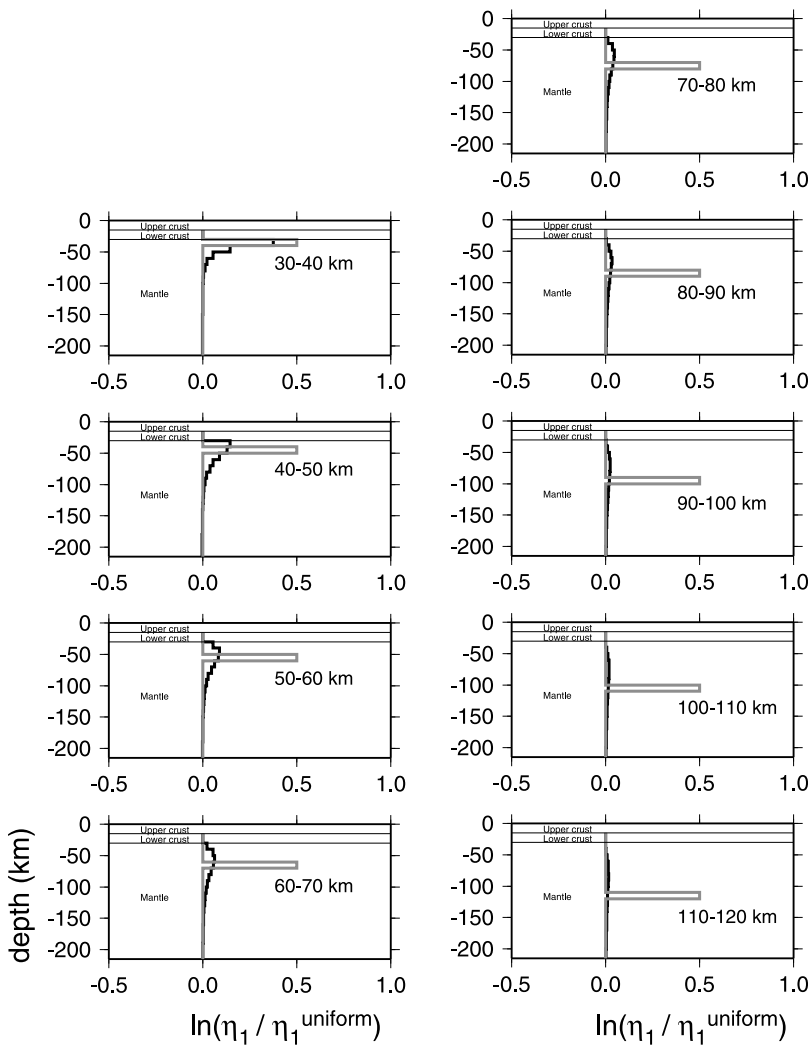

Figure 12. Subset of the model resolution matrix for layered steady state mantle viscosity, using the class III model. Each plot represents a row of the matrix **R** given by equation (22). The elements of the matrix are depicted as inverted layer values (black curves) resulting from an input layer perturbation of amplitude 0.5 in logarithmic viscosity (indicated in gray).

gradient in logarithmic viscosity and define $\mathbf{p}_\gamma$ as the viscosity profile given by

$$\ln \eta_1(r) = \ln \eta_1(r_0) - \gamma(r - r_0), \tag{23}$$

where r_0 = 6341 km is the Moho radius. The differenced model velocity on $\mathbf{p}_\gamma$ is

$$\begin{aligned}\Delta v^k_{\mathrm{mod}}(\hat{\mathbf{r}}_n, l; \mathbf{p}_\gamma) \approx{}& \Delta v^k_{\mathrm{mod}}(\hat{\mathbf{r}}_n, l; \mathbf{p}_0) \\ &+ \sum_j \left[\ln\left(\frac{\eta_1(r_0)}{\eta_1^{\mathrm{uniform}}}\right) - \gamma(\bar{r}_j - r_0)\right] \\ &\cdot \partial_{\epsilon_j} \Delta v^k_{\mathrm{mod}}(\hat{\mathbf{r}}_n, l; \mathbf{v})|_{\mathbf{v}=\mathbf{p}_0},\end{aligned} \tag{24}$$

where $\bar{r}_j = (1/2)(r_1^{(j)} + r_2^{(j)})$.

[38] For each model class, the observed velocity fields are inverted by least squares for optimal ln $\eta_1(r_0)$ and γ by minimizing χ^2_{total} (equation (13)). The resulting ln $\eta_1(r)$ relative to ln $\eta_1^{\mathrm{uniform}}$ are shown in Figure 13. Model class I exhibits a decrease in mantle viscosity by a factor of ~1.5 from the Moho to 220 km depth. The error bounds indicate that at the 95% confidence level, the negative gradient with depth (γ = −0.0041 ± 0.0012/km) is significantly different from zero. Similarly, the positive viscosity gradient for class II (0.0061 ± 0.0014/km) is significantly different from zero. However, the viscosity gradient is not significantly different from zero for class III (0.0025 ± 0.0016/km). Since the class II and III models differ only in the finiteness of lower crust viscosity for class III, this indicates a trade-off with the lower crust viscosity.

7.2. Unrestricted Layering in Mantle Viscosity

[39] Since the model of a Maxwellian mantle (class I) provides a relatively poor fit to the postseismic data (Figure 6 and Table 1), we consider unrestricted layering in mantle viscosity in the context of class II and III models. Logarithmic mantle viscosity is parameterized with equation (16) in 19 layers of uniform thickness between 30 and 220 km depth, and the solution for depth-dependent viscosity is given by equation (20).

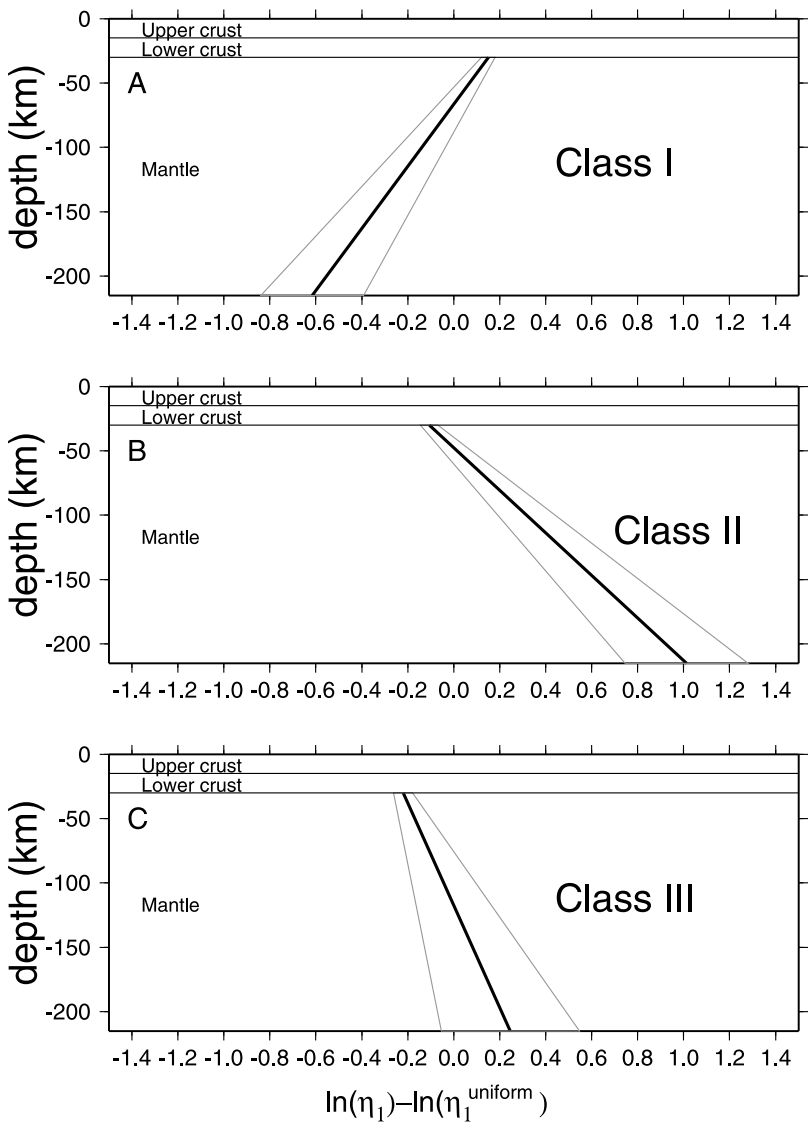

Figure 13. Depth-dependent steady state viscosity $\ln \eta_1(r)$ relative to uniform viscosity $\ln \eta_1^{\text{uniform}}$ resulting from least squares inversion of the observed velocity field (Figure 1) using a linear gradient with depth for logarithmic viscosity (equation (23)). Error bounds (±1 standard deviation about the plotted values) are shown with adjacent gray lines.

[40] Estimated viscosity structures obtained from the inversions using Fréchet derivatives evaluated on model classes II and III are shown in Figure 14. Both model classes II and III show a similar tendency for reduced mantle viscosity in the upper 10 km of the mantle, with an abrupt viscosity increase in a 20 km thick layer in the underlying mantle and uniform (and lower) viscosity below 70 km depth. If real, these layered structures would suggest that the gentle viscosity gradients estimated in the simpler models of section 7.1 represent an average of alternating high- and low-viscosity layers in the upper ~50 km of the mantle. The data fit patterns in Figure 6 and Table 1 show that there is little improvement in data fit between a model with uniform viscosity or a constant viscosity gradient and one with unrestricted layering. However, formal F tests [e.g., *Bevington*, 1969] would suggest that the significance of the layered model over both the uniform-viscosity and the viscosity gradient model is nearly 100%. These significance tests assume, based on the analysis of section 6, that the layered model involves effectively two degrees of freedom. Such significance tests are independent of the absolute scaling of the data errors and therefore do not inform on whether the inferred perturbations are significantly different from zero. The perturbations associated with the layered structures in Figure 14 are, at the 95% confidence level, significantly different from zero only for the shallowest mantle layer, that from 30–40 km depth. The discussion below strongly suggests that those perturbations are strongly dependent on the selection of data, so that the formal model errors are only a rough guide.

8. Discussion

8.1. Time Dependence of Baseline Shift

[41] The baseline shift applied to the observed velocity field for each time interval, derived from fitting the relaxa-

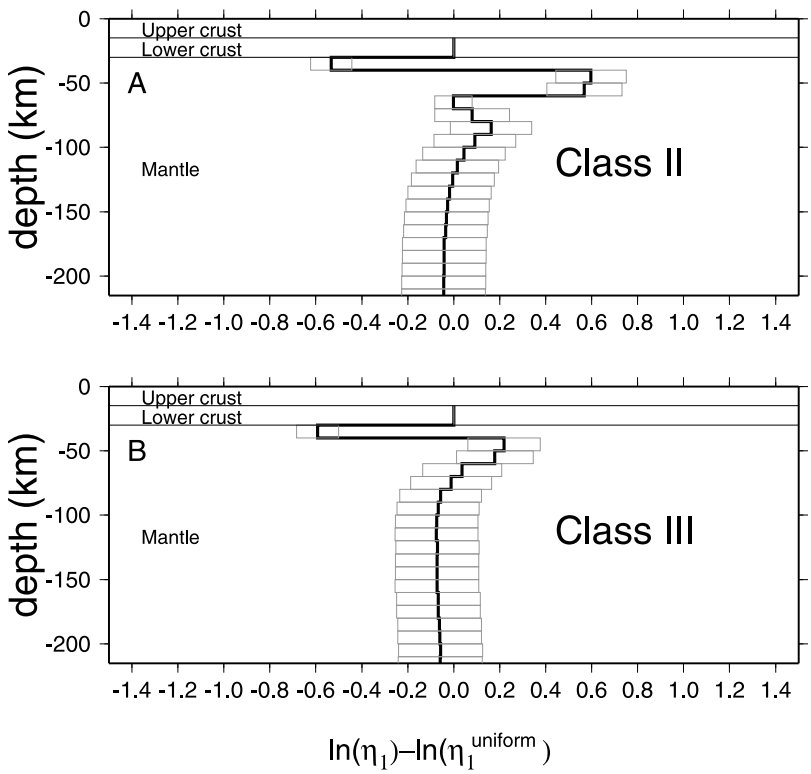

Figure 14. Same as Figure 13 but with unrestricted variation in depth-dependent viscosity $\eta_1(r)$, parameterized with 19 mantle layers (section 7.2).

tion model, is given in Figure 3. As discussed in section 2, baseline shifts of order 1–2 mm/yr are consistently seen in the east component. They are much smaller in the north component with the exception of the 2 weeks to 6 months time interval, where the north component shift is 1.68 mm/yr. The net baseline shift for that time interval acts, in particular, to rotate observed south directed postseismic velocity vectors in the northern part of the study area by ~40° degrees clockwise while preserving a net postseismic velocity of ~2–3 mm/yr (compare Figures 1 and 9). Although the origin of this shift is uncertain, Figure 3 strongly suggests that it is time dependent. This is verified by evaluating the model U performance over the time interval 2 weeks to 5 years, which spans all the time intervals represented in Figure 3. The model fit is shown in Figure 15. The resulting baseline velocity shift is (−0.4 mm/yr east, −0.2 mm/yr north), showing that long-term observational bias is smaller than that over shorter time intervals.

8.2. Influence of Alternative Processes

[42] Sites within a fault length of the Hector Mine rupture may be affected by other postseismic processes, chiefly poroelastic (PE) rebound and after slip. These processes are generally operating jointly with viscoelastic relaxation [e.g., *Jónsson et al.*, 2003; *Fialko*, 2004; *Savage et al.*, 2005; *Freed et al.*, 2006; *Perfettini and Avouac*, 2007; *Jónsson*, 2008; *Han and Stein*, 2009; *Hearn et al.*, 2009], and the question arises as to the relative importance of these processes in a particular tectonic setting, as well as their respective time dependences. Under the supposition that far-field sites are affected predominantly by viscoelastic relaxation of the lower crust and mantle, we repeat the preceding inversions for layered mantle viscosity structure but exclude the near-field sites defined by *Freed et al.* [2007] (i.e., those less than 50 km from the 1992 and 1999 ruptures). The results (Figure 16) exhibit much smaller apparent variations in viscosity with depth compared with the results that include the near-field sites (Figure 14). Although slightly reduced viscosity from 30–40 km depth remains, there is no pronounced low-viscosity channel from 30–40 km depth, indicating that the inference of such a feature in Figure 14 depends on the contributions of near-field data, which are likely to be sensitive to near-field processes that we do not account for.

[43] In order to test the potential impact of near-field processes on the postseismic deformation fields, we construct simple models of them. For PE rebound, we assume that postseismic deformation represents the transition for undrained to drained conditions with associated reduction of Poisson's ratio ν [*Peltzer et al.*, 1998]. The differenced coseismic displacement fields using the drained and undrained values yields an estimate of the total available contribution of PE rebound. For after slip, we construct a model of unit right-lateral slip distributed in the depth range 15–30 km beneath the Hector Mine coseismic rupture planes. Comparison of either the PE or after slip models with model U residuals in various time intervals (i.e., the residuals resulting from the model presented in section 5.2 and Figure 9) yields the relative importance of either process as a function of time. With a drained Poisson's ratio of 0.27, and with trial values over a wide range of undrained ν (representing effective time-dependent Poisson's ratio),

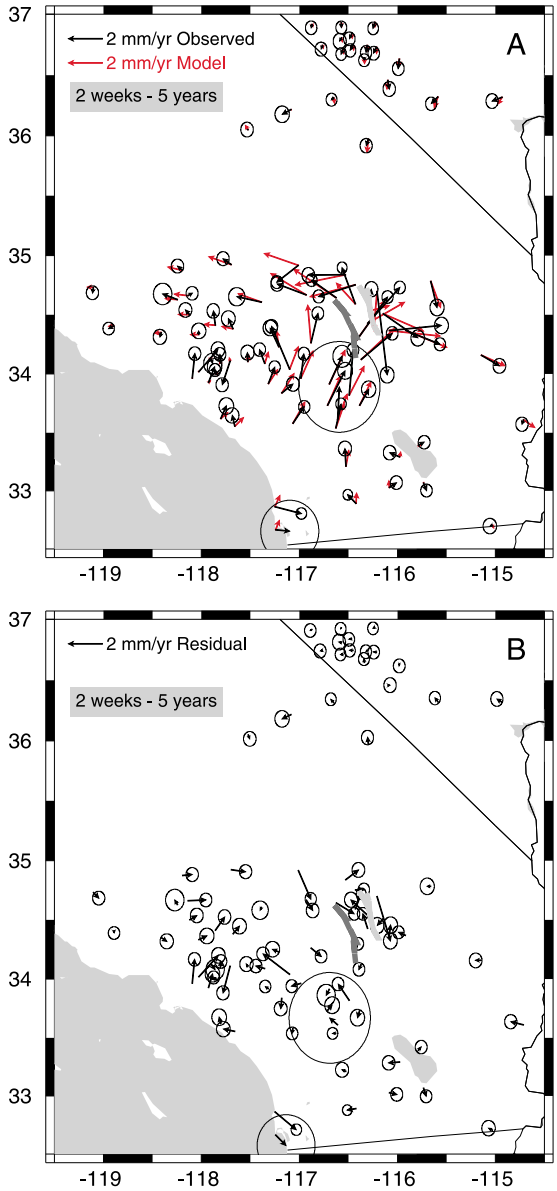

Figure 15. (a) Observed differenced horizontal velocity field for the 2 weeks to 5 years time interval, given by equation (8) and corrected for a baseline shift (equation (11)). Error ellipses are 95% confidence regions. Red vectors are the corresponding predictions of model U (section 5.2). (b) Residual velocity field (observed minus model velocity field).

we find that there is negligible correlation of the PE deformation fields with model U residuals and correspondingly negligible improvement in NRMS.

[44] However, the after slip velocity field is moderately correlated with the model U residuals in all but the latest time period. Its coherence with the residual velocity field is 0.21 (2 weeks to 6 months), 0.48 (6 months to 1 year), 0.20 (1 year to 2 years), and 0.01 (2 years to 5 years). The after slip rates which best fit the residuals are shown in Figure 17 together with NRMS of model U and model U appended with after slip. The improvement in fit with inclusion of after slip is statistically significant over all time intervals up to 2 years, but especially during 6 months to 1 year. This may indicate a real peak in after slip rate during this time interval or, alternatively, an inaccurate rheology combined with a monotonically decreasing after slip rate that mimics the derived apparent after slip rate. Note that a very different choice of viscosities, represented by the square symbols in Figure 7, yields a better fit to the 6 months to 1 year velocity field (NRMS = 1.55 versus NRMS = 1.65 for model U), suggesting that a more complicated rheology such as the VEVE model of *Ivins* [1996] or biviscous rheology in both the lower crust and mantle may be needed to explain the postseismic relaxation over the entire spectrum of times considered.

[45] Since the baseline shift is so small for the 2 weeks to 5 years time interval (section 8.1), the pattern of residuals may be interpreted with physical processes. NRMS using all GPS sites is 3.25 and 2.97 with near-field sites excluded, showing that far-field residuals are systematically smaller. This is consistent with minor after slip over this time interval, as suggested previously in Figure 17. The 2 weeks to 5 years model fit in Figure 15a in the far field is comparable with that achieved by the *Freed et al.* [2007] viscoelastic relaxation model for the first 7 years (i.e., similar unweighted root-mean-square misfit of order 1 mm/yr), which considered only far-field data.

[46] The formally large NRMS for all time periods considered is worse than that typically achieved by models of interseismic deformation. This is likely due to the complexity of postearthquake relaxation, which involves more than one process with likely different time dependences. Such large NRMS values, however, appear typical for postearthquake relaxation studies [e.g., *Hearn et al.*, 2009]. A possible bias in our NRMS may result from the assumption of white noise used to derive the interval velocity estimates in section 2. A velocity estimation procedure that involves correlated noise (e.g., fractal random walk, flicker noise) yields standard deviations in interval velocities up to 3–6 times larger than those resulting from the assumption of white noise [*Zhang et al.*, 1997]. NRMS would be correspondingly reduced and may be closer to unity than listed in Table 1.

8.3. Implications for Yucca Mountain Area

[47] The northern part of the study area encompasses the Yucca Mountain area. Right-lateral shear strain rates of ~20 nanostrain (nstrain)/yr have been interpreted by *Wernicke et al.* [2004] as indicative of about 1 mm/yr strain accumulation on local strike-slip faults, which would imply a recurrence interval of a few thousands of years. Since the observations of *Wernicke et al.* [2004] span the 4 years following the 1999 Hector Mine earthquake, the question arises as to how much of the active shear arises from lower crust and mantle relaxation following the Hector Mine earthquake.

[48] The curvature of observed time series in this region (MERC and SMYC in Figure 10) during the first postseismic year cannot be explained by local processes [e.g., *Hammond et al.*, 2010] and demand viscoelastic relaxation of the lower crust and mantle. We find that the postseismic velocity field is explained to a large extent by this relaxation (Figure 18). The variance reduction of model U to the observed velocity in the region (those sites north of 35.5°N) is: 71% (2 weeks to 6 months), 31% (6 months to 1 year),

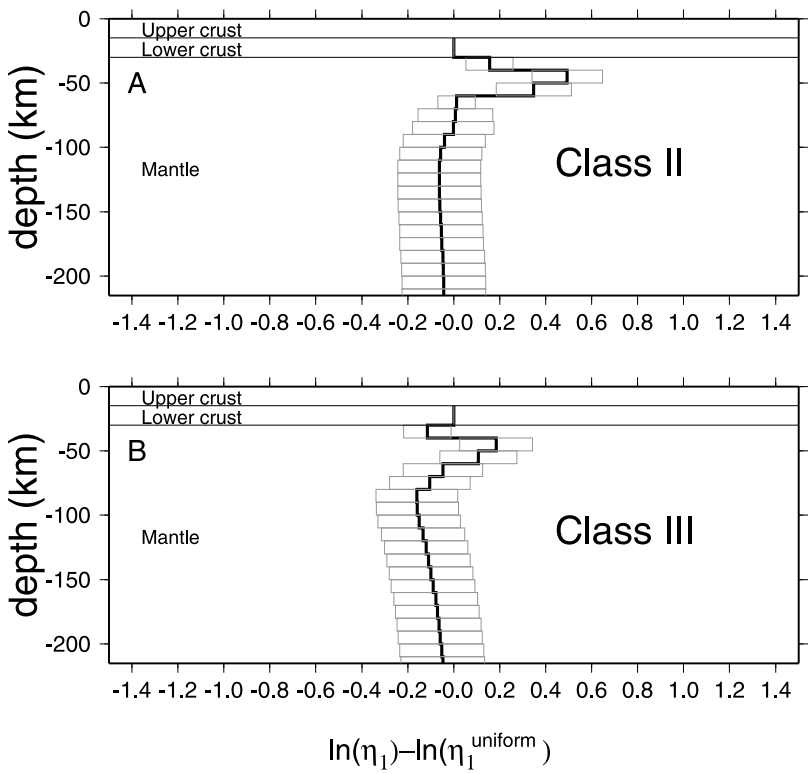

Figure 16. Same as Figure 14, but observations are restricted to far-field sites.

47% (1 year to 2 years), and 24% (2 years to 5 years). Bearing in mind that our velocities (both observed and modeled) are referenced to the respective velocities in the 5–9 year postseismic time interval, observed maximum engineering shear strain rates in the Yucca Mountain area decrease from ~20 to 10 nstrain/yr during the first two postseismic years; the model U decrease is from ~20 to 5 nstrain/yr during the first 2 years. However, the azimuth of the observed maximum shear differs typically by about 50° from the corresponding model U orientations. Thus, while model U predicts the observed velocities and strain rate magnitudes in the Yucca Mountain region, it does not replicate the azimuth of maximum shear. The inference of tectonic strain not explicable with postearthquake relaxation is consistent with a detailed study by *Hammond et al.* [2010].

8.4. Remarks on Resolution of η_1

[49] The model resolution suggests that details of mantle viscosity structure are resolved on a vertical scale of ~10–20 km at depth $\lessapprox$ 60 km, but that deeper viscosity variations are poorly resolved. This is supported by the fact that at most two eigenvalues contribute significantly to the overall solution for depth-dependent logarithmic viscosity. The eigenvectors associated with the two largest eigenvalues are concentrated in the 30–80 km depth range in the mantle.

[50] We may test whether trade-offs with other model parameters affect the layered mantle viscosity structures estimated for model classes II and III. In the context of the layered model, we obtained the corresponding viscosity structures resulting when depth-dependent η_1 is estimated jointly with a depth-independent perturbation in η_2 and/or η_c. Resulting perturbations in these parameters are small (less than 10%) and viscosity variations with depth differ negligibly from those shown in Figure 14.

[51] For any of the gradient models of section 7.1 or layered models of section 7.2, residual misfit is slightly improved relative to a model of constant steady state mantle viscosity (Figure 6). Formal F tests indicate that within class III, a model with either a constant gradient in

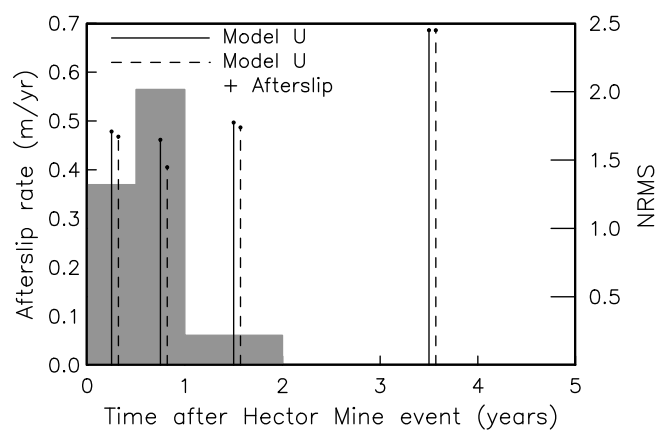

Figure 17. Best fitting time-dependent after slip rate (shaded region) in four postseismic time intervals, derived from fitting model U residuals, and corresponding NRMS without after slip (solid vertical line segments, identical to model U entries in Table 1) and with after slip (dashed vertical line segments). The rate is <0.01 m/yr in the 2–5 year time interval.

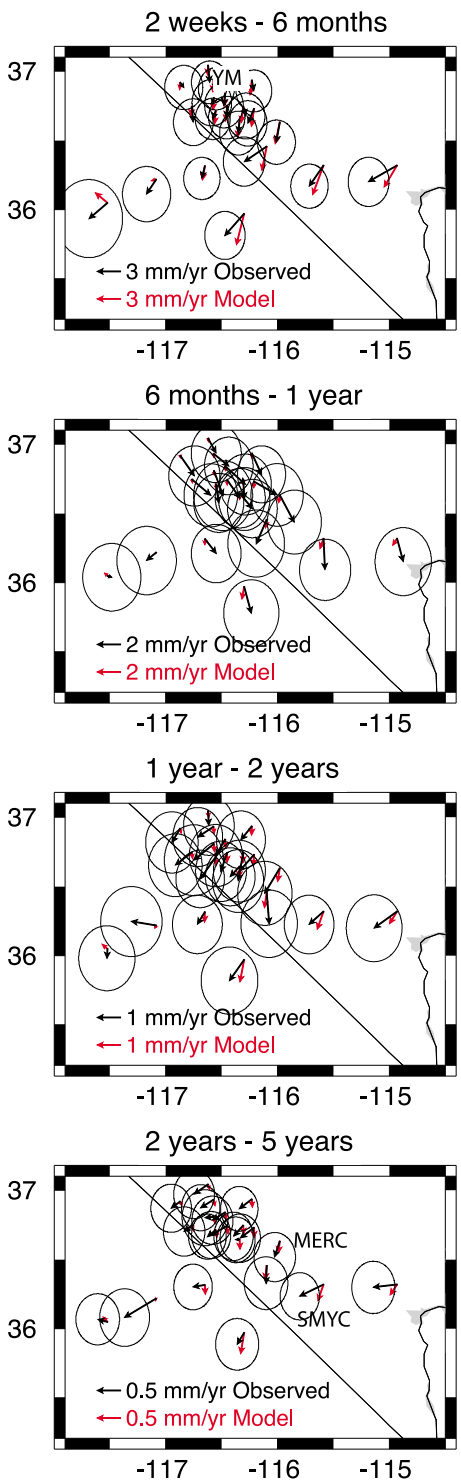

Figure 18. Same as Figure 9 but replotted in the Yucca Mountain region (location indicated with YM).

logarithmic viscosity or a multilayered mantle viscosity structure (Figures 6 and 8) performs better than a model with a constant mantle viscosity, i.e., model U, at nearly 100% significance. However, after the absolute data errors are propagated through the inversion procedure, the resulting error bounds associated with these two models (Figures 13c, 14b, and 16b) imply that little or no variation in mantle viscosity with depth is warranted by the data.

8.5. Alternative Viscoelastic Relaxation Models

[52] Applying a variation of the two-dimensional *Savage and Prescott* [1978] viscoelastic coupling model to the interseismic velocity field and post-Landers deformation around the southern San Andreas fault, *Johnson et al.* [2007] derived a viscoelastic stratification involving a relatively high-viscosity lower crust (15–30 km depth), high-viscosity uppermost mantle (i.e., strong mantle lid at 30–50 km depth), and an underlying low-viscosity mantle. Figure S6 shows the predicted horizontal velocity fields on the *Johnson et al.* [2007] viscoelastic structure (presented in their Figure 7). Since the model does not contain either a weak lower crust or a transient mantle viscosity, predicted velocities are much smaller than observed during the first year. A possible way to remedy this would be to introduce after slip during the first year. We find that 30 cm of after slip distributed in the depth range 15–30 km beneath the Hector Mine coseismic rupture planes is sufficient to approximately match the horizontal displacement field during the first year. However, such an after slip model produces a vertical velocity pattern during the first 6 months (Figure 2c) of much greater amplitude than that predicted from postseismic relaxation on the *Johnson et al.* [2007] model (Figure 2d) and that is anticorrelated with the observed vertical velocity field (Figure 2a). The chief differences of the *Johnson et al.* [2007] model with those of the present study (e.g., model U) are the presence of a strong mantle lid and lack of a transient viscosity. If both models are appropriate for their respective study areas, then the contrasting models imply considerable lateral variation in depth-dependent viscosity across southern California.

[53] In their study of the first 7 years of GPS data after the Hector Mine earthquake, *Freed et al.* [2007] asserted that the data require a strong mantle lid (the upper ~10–20 km of the mantle) underlain by a weak mantle. Our inversions for layered structure, which do not exhibit relatively high viscosity in the upper 10 km of the mantle, do not support this claim (Figures 14 and 16). We further test the hypothesis of a strong mantle lid by repeating the grid search of section 5.2 for best fitting η_1 and ratio η_2/η_1 with the constraint that η_1 in the depth range 30–40 km be ten times greater than that at greater depth. The results in Figure S7 are consistent with optimal viscosity parameters $\eta_1 = 2.8 \times 10^{18}$ Pa s and $\eta_2 = 0.06 \times \eta_1 = 1.7 \times 10^{17}$ Pa s (Figure 8d). NRMS in specific time periods (Table 1), as well as overall NRMS using this viscosity structure (squares in class III results plotted in Figure 6), are worse than those of the gradient model and layered viscosity model.

9. Conclusions

[54] We consider 9 years of crustal motions in southern California following the 1999 Hector Mine earthquake in order to constrain the mantle viscosity structure. SOPAC time series provided by NASA's REASON project are used for this purpose. Previous work shows that the postseismic crustal motions are dominated by viscoelastic relaxation of the mantle. In order to explain the rapidly diminishing amplitude of postseismic crustal velocity with time, effec-

tive mantle viscosity must increase with time [*Pollitz et al.*, 2001; *Pollitz*, 2003; *Freed and Bürgmann*, 2004]. This property demands some form of transient rheology, e.g., a nonlinear (stress and temperature-dependent) rheology or a linear rheology with more than one material relaxation time. Following *Pollitz* [2003] we adopt the latter model and represent the mantle rheology with a Jeffreys fluid (Burgers body with equal transient and steady state rigidities). The long time series in both horizontal and vertical motions potentially constrain depth-dependent steady state mantle viscosity.

[55] A formal resolution analysis shows that at most two independent constructs of steady state mantle viscosity may be resolved by the postearthquake data set. Depth variations in steady state viscosity can be resolved at a ~10–20 km scale down to at most ~60 km depth, and resolution is poor at greater depth.

[56] Even without considering the depth dependence, precise details of the transient rheology are difficult to extract from a data set limited to surface observations. In the context of the Jeffreys fluid, a very different combination of viscosities (approximately 10 times greater) fits the data set almost as well as the those viscosities employed in our analysis.

[57] Any of the models shown in Figure 8 provide a satisfactory fit to the data. The two models of Figures 8b and 8c, with depth-dependent mantle viscosity, provide slightly better fits than that of Figure 8a with uniform mantle viscosity; the mantle lid model of Figure 8d performs worse. In general, models involving either a simple linear gradient in logarithmic steady state viscosity with depth or more general layering suggest a weak viscosity increase with depth, but such an increase is not significant at the level of two standard deviations in estimated vertical viscosity variation. The lack of detectable viscosity variations with depth suggests that the viscosity in the uppermost mantle may not exhibit the temperature dependence predicted by laboratory measurements and extrapolated to geologic strain rates [e.g., *Thatcher and Pollitz*, 2008, Figure 2]. This suggests a counterbalancing role of additional factors such as grain size or fugacities of interstitial or intracrystalline components. For example, an increase in grain size with increasing depth in the diffusion creep regime [e.g., *Bürgmann and Dresen*, 2008] would act to increase viscosity with increasing depth deeper than 50 km and counterbalance the viscosity decrease expected from the temperature increase with depth.

[58] Our analysis is generally applicable to other data sets of postseismic relaxation. Other applications may have the same limitations as the present study, e.g., the ambiguity between viscoelastic relaxation and other postseismic processes, the use of only surface observations, and the limited time span of the observations. The latter point is particularly important if the goal is to constrain "steady state" mantle viscosity, for which a 9 year long record is probably too short. On the other hand, resolution may be improved in other cases where more vertical constraints (such as InSAR) are available.

[59] **Acknowledgments.** This study makes use of data made available by NASA through the REASoN Project (http://reason.scign.org/scignDataPortal/). We thank the Associate Editor and three anonymous reviewers, and internal reviewers Jim Savage, Jessica Murray-Moraleda, and John Langbein, for their careful reading and constructive criticisms of this work.

References

Altamimi, Z., X. Collilieux, J. Legrand, B. Garayt, and C. Boucher (2007), ITRF2005: A new release of the International Terrestrial Reference Frame based on time series of station positions and Earth Orientation Parameters, *J. Geophys. Res.*, *112*, B09401, doi:10.1029/2007JB004949.

Bevington, P. R. (1969), *Data Reduction and Error Analysis for the Physical Sciences*, McGraw-Hill, New York.

Bills, B. G., D. R. Currey, and G. A. Marshall (1994a), Viscosity estimates for the crust and upper mantle from patterns of lacustrine shoreline deformation in the Eastern Great Basin, *J. Geophys. Res.*, *99*, 22,059–22,086, doi:10.1029/94JB01192.

Bills, B. G., S. L. de Silva, D. R. Currey, R. S. Emenger, K. D. Lillquist, A. Donnellan, and B. Worden (1994b), Hydro-static deflection and tectonic tilting in the central Andes: Initial results of a GPS survey of Lake Minchin shorelines, *Geophys. Res. Lett.*, *21*, 293–296, doi:10.1029/93GL03544.

Bills, B. G., K. D. Adams, and S. G. Wesnousky (2007), Viscosity structure of the crust and upper mantle in western Nevada from isostatic rebound patterns of the late Pleistocene Lake Lahontan high shoreline, *J. Geophys. Res.*, *112*, B06405, doi:10.1029/2005JB003941.

Bürgmann, R., and G. Dresen (2008), Rheology of the lower crust and upper mantle: Evidence from rock mechanics, geodesy, and field observations, *Annu. Rev. Earth Planet. Sci.*, *36*, 531–567, doi:10.1146/annurev.earth.36.031207.124326.

Carter, N. L., and S. Kirby (1978), Transient creep and semi-brittle behavior of crystalline rocks, *Pure Appl. Geophys.*, *116*, 807–839, doi:10.1007/BF00876540.

Fialko, Y. (2004), Evidence of fluid-filled upper crust from observations of postseismic deformation due to the 1992 M_w7.3 Landers earthquake, *J. Geophys. Res.*, *109*, B08401, doi:10.1029/2004JB002985.

Freed, A. M., and R. Bürgmann (2004), Evidence of powerlaw flow in the Mojave Desert mantle, *Nature*, *430*, 548–551, doi:10.1038/nature02784.

Freed, A. M., R. Bürgmann, E. Calais, J. Freymueller, and S. Hreinsdóttir (2006), Implications of deformation following the 2002 Denali, Alaska, earthquake for postseismic relaxation processes and lithospheric rheology, *J. Geophys. Res.*, *111*, B01401, doi:10.1029/2005JB003894.

Freed, A. M., R. Bürgmann, and T. Herring (2007), Far-reaching transient motions after Mojave earthquakes require broad mantle flow beneath a strong crust, *Geophys. Res. Lett.*, *34*, L19302, doi:10.1029/2007GL030959.

Hammond, W. C., C. Kreemer, and G. Blewitt (2008), Geodetic constraints on contemporary deformation in the northern Walker Lane: 3, Central Nevada Seismic Belt postseismic relaxation, in *Late Cenozoic Structure and Evolution of the Great Basin-Sierra Nevada Transition*, edited by J. S. Oldow and P. H. Cashman, *Spec. Pap. Geol. Soc. Am.*, *447*, 33–54, doi:10.1130/2009.2447(03).

Hammond, W. C., C. Kreemer, G. Blewitt, and H.-P. Plag (2010), Effect of viscoelastic postseismic relaxation on estimates of interseismic crustal strain accumulation at Yucca Mountain, Nevada, *Geophys. Res. Lett.*, *37*, L06307, doi:10.1029/2010GL042795.

Han, C.-H., and R. S. Stein (2009), Stress evolution following the 1999 Chi-Chi, Taiwan, earthquake: consequences for afterslip, relaxation, aftershocks and departures from Omori decay, *Geophys. J. Int.*, *177*, 179–192, doi:10.1111/j.1365-246X.2008.04069.x.

Hearn, E. H., S. McClusky, S. Ergintav, and R. E. Reilinger (2009), Izmit earthquake postseismic deformation and dynamics of the North Anatolian Fault Zone, *J. Geophys. Res.*, *114*, B08405, doi:10.1029/2008JB006026.

Ingebritsen, S. E., and C. E. Manning (1999), Geological implications of a permeability-depth curve for the continental crust, *Geology*, *27*, 1107–1110, doi:10.1130/0091-7613(1999)027<1107:GIOAPD>2.3.CO;2.

Ivins, E. R. (1996), Transient creep of a composite lower crust, 1, constitutive theory, *J. Geophys. Res.*, *101*, 27,981–28,004, doi:10.1029/96JB02847.

Johnson, K. M., G. E. Hilley, and R. Bürgmann (2007), Influence of lithosphere viscosity structure on estimates of fault slip rate in the Mojave region of the San Andreas fault system, *J. Geophys. Res.*, *112*, B07408, doi:10.1029/2006JB004842.

Jónsson, S. (2008), Importance of post-seismic viscous relaxation in southern Iceland, *Nat. Geosci.*, *1*, 136–139, doi:10.1038/ngeo105.

Jónsson, S., H. Zebker, P. Segall, and F. Amelung (2002), Fault slip distribution of the 1999 M_w 7.1 Hector Mine, California, earthquake, estimated from satellite radar and GPS measurements, *Bull. Seismol. Soc. Am.*, *92*, 1377–1389, doi:10.1785/0120000922.

Jónsson, S., P. Segall, R. Pedersen, and G. Björnsson (2003), Post-earthquake ground movements correlated to pore-pressure transients, *Nature*, *424*, 179–183, doi:10.1038/nature01776.

Kaufmann, G., and F. Amelung (2000), Reservoir-induced deformation and continental rheology in the vicinity of Lake Mead, Nevada, *J. Geophys. Res.*, *105*, 16,341–16,358, doi:10.1029/2000JB900079.

Kaufmann, G., and K. Lambeck (2000), Mantle dynamics, postglacial rebound and the radial viscosity profile, *Phys. Earth Planet. Inter.*, *121*, 301–324, doi:10.1016/S0031-9201(00)00174-6.

Kendall, R. A., and J. X. Mitrovica (2007), Radial resolving power of far-field differential sea-level highstands in the inference of mantle viscosity, *Geophys. J. Int.*, *171*, 881–889, doi:10.1111/j.1365-246X.2007.03546.x.

Lambeck, K., and M. Nakada (1990), Late Pleistocene and Holocene sea level change along the Australian coast, *Palaeogeogr. Palaeoclimatol. Palaeoecol.*, *89*, 143–176, doi:10.1016/0031-0182(90)90056-D.

Langbein, J. (2004), Noise in two-color electronic distance meter measurements revisited, *J. Geophys. Res.*, *109*, B04406, doi:10.1029/2003JB002819.

Langbein, J., and H. Johnson (1997), Correlated errors in geodetic time series: Implications for time-dependent deformation, *J. Geophys. Res.*, *102*, 591–603, doi:10.1029/96JB02945.

Mao, A., C. G. A. Harrison, and T. H. Dixon (1999), Noise in GPS coordinate time series, *J. Geophys. Res.*, *104*, 2797–2816, doi:10.1029/1998JB900033.

Menke, W. (1989), *Geophysical Data Analysis: Discrete Inverse Theory*, *Int. Geophys. Ser.*, vol. 45, Academic, San Diego, Calif.

Mitrovica, J. X., and W. R. Peltier (1991), A complete formalism for the inversion of post-glacial rebound data: Resolving power analysis, *Geophys. J. Int.*, *104*, 267–288, doi:10.1111/j.1365-246X.1991.tb02511.x.

Nakada, M., and K. Lambeck (1989), Late Pleistocene and Holocene sea-level change in the Australian region and mantle rheology, *Geophys. J. Int.*, *96*, 497–517, doi:10.1111/j.1365-246X.1989.tb06010.x.

Owen, S., G. Anderson, D. C. Agnew, H. Johnson, K. Hurst, R. Reilinger, Z.-K. Shen, J. Svarc, and T. Baker (2002), Early postseismic deformation from the 16 October 1999 M_w 7.1 Hector Mine, California, earthquake as measured by survey-mode GPS, *Bull. Seismol. Soc. Am.*, *92*, 1423–1432, doi:10.1785/0120000930.

Peltzer, G., P. Rosen, F. Rogez, and K. Hudnut (1998), Poroelastic rebound along the Landers 1992 earthquake surface rupture, *J. Geophys. Res.*, *103*, 30,131–30,145, doi:10.1029/98JB02302.

Perfettini, H., and J.-P. Avouac (2007), Modeling afterslip and aftershocks following the 1992 Landers earthquake, *J. Geophys. Res.*, *112*, B07409, doi:10.1029/2006JB004399.

Pollitz, F. F. (1997), Gravitational viscoelastic postseismic relaxation on a layered spherical Earth, *J. Geophys. Res.*, *102*, 17,921–17,941, doi:10.1029/97JB01277.

Pollitz, F. F. (2003), Transient rheology of the uppermost mantle beneath the Mojave Desert, California, *Earth Planet. Sci. Lett.*, *215*, 89–104, doi:10.1016/S0012-821X(03)00432-1.

Pollitz, F. F., C. Wicks, and W. Thatcher (2001), Mantle flow beneath a continental strike-slip fault: Postseismic deformation after the 1999 Hector Mine earthquake, *Science*, *293*, 1814–1818, doi:10.1126/science.1061361.

Post, R. L. (1977), High-temperature creep of Mt. Burnet Dunite, *Tectonophysics*, *42*, 75–110, doi:10.1016/0040-1951(77)90162-7.

Ranalli, G. (1987), *Rheology of the Earth: Deformation and Flow Processes in Geophysics and Geodynamics*, vol. 1, Allen and Unwin, Boston, Mass.

Riva, R. E. M., and R. Govers (2009), Relating viscosities from postseismic relaxation to a realistic viscosity structure for the lithosphere, *Geophys. J. Int.*, *176*, 614–624, doi:10.1111/j.1365-246X.2008.04004.x.

Savage, J. C., and W. H. Prescott (1978), Asthenospheric readjustment and the earthquake cycle, *J. Geophys. Res.*, *83*, 3369–3376, doi:10.1029/JB083iB07p03369.

Savage, J. C., and J. L. Svarc (1997), Postseismic deformation associated with the 1992 M_w = 7.3 Landers earthquake, southern California, *J. Geophys. Res.*, *102*, 7565–7577, doi:10.1029/97JB00210.

Savage, J. C., J. L. Svarc, and S.-B. Yu (2005), Postseismic relaxation and transient creep, *J. Geophys. Res.*, *110*, B11402, doi:10.1029/2005JB003687.

Shen, Z.-K., D. Jackson, and B. Ge (1996), Crustal deformation across and beyond the Los Angeles Basin from geodetic measurements, *J. Geophys. Res.*, *101*, 27,957–27,980, doi:10.1029/96JB02544.

Thatcher, W., and F. F. Pollitz (2008), Temporal evolution of continental lithospheric strength in actively deforming regions, *GSA Today*, *18*, 4–11, doi:10.1130/GSAT01804-5A.1.

Wald, D., and T. Heaton (1994), Spatial and temporal distribution of slip for the 1992 Landers, California, earthquake, *Bull. Seismol. Soc. Am.*, *84*, 668–691.

Wernicke, B., J. L. Davis, R. A. Bennett, J. E. Normandeau, A. M. Friedrich, and N. A. Niemi (2004), Tectonic implications of a dense continuous GPS velocity field at Yucca Mountain, Nevada, *J. Geophys. Res.*, *109*, B12404, doi:10.1029/2003JB002832.

Wiggins, R. A. (1972), The general linear inverse problem: Implications of surface waves and free oscillations for earth structure, *Rev. Geophys.*, *10*, 251–285, doi:10.1029/RG010i001p00251.

Williams, S. D. P. (2003), The effect of coloured noise on the uncertainties of rates estimated from geodetic time series, *J. Geod.*, *76*, 483–494, doi:10.1007/s00190-002-0283-4.

Zhang, J., Y. Bock, H. Johnson, P. Fang, S. Williams, J. Genrich, S. Wdowinski, and J. Behr (1997), Southern California Permanent Geodetic Array: Error analysis of daily position estimates and site velocities, *J. Geophys. Res.*, *102*, 18,035–18,055, doi:10.1029/97JB01380.

F. F. Pollitz and W. Thatcher, U.S. Geological Survey, 345 Middlefield Rd., MS 977, Menlo Park, CA 94025, USA. (fpollitz@usgs.gov)